

# UNIVERSITÀ DEGLI STUDI DI PADOVA

Dipartimento di Fisica e Astronomia “Galileo Galilei”

Corso di Laurea Magistrale in Fisica

## Phase I of the ANNIE experiment: Data Acquisition system and preliminary data analysis

### RELATORE

Dott. Gianmaria Collazuol

### CANDIDATO:

Tommaso Boschi  
*matr.* 1105506

### CORRELATORI:

Prof. Francesca Di Lodovico (QMUL)

Dr. Benjamin Richards (QMUL)



*Agli amici più grandi.  
A chi ho perso per strada.*



# Overview

This thesis is placed within the context of the The Accelerator Neutrino Neutron Interaction Experiment (ANNIE), a water Cherenkov detector built at the Fermi National Accelerator Laboratory. The main aim of ANNIE is to study in depth the nature of neutrino-nucleus interactions by analysing the yield of final state neutrons produced in this kind of interactions. New technologies, such as gadolinium-loaded water and, for the first time, Large Area Picosecond Photodetectors (LAPPDs) will be also employed in future phases of the experiment. The measurement will have relevant implications for next generation Water Cherenkov detectors, in that these techniques may play a significant role in reducing backgrounds in relation to proton decay measurements, supernova neutrino observations and neutrino interaction physics.

This paper deals with the Phase I of the experiment, in which photomultipliers (PMT) are adopted within the tank and the forward Veto and the Muon Range Detector (MRD) are partially being employed. A small container, called Neutron Volume Capture (NVC) is also inside the tank, for preliminary neutron yield studies. The main work of the thesis consists of the development of the CAMAC electronics Data Acquisition system (DAQ); the already existing VME electronics DAQ, for the water PMTs, is also described. Furthermore, early stage data are analysed and studied, and event reconstruction techniques are proposed.

All the described activities were undertaken in the Particle Physics Research Group of the Queen Mary University of London.

This thesis is divided as follows:

**Chapter 1** Neutrino Physics is briefly introduced and the experimental techniques for their detection are listed.

**Chapter 2** The ANNIE Experiment is described.

**Chapter 3** The DAQ system is illustrated, as long as future developments.

**Chapter 4** Data analysis techniques, mainly focused on signal/noise discrimination, are shown. Event reconstruction is also taken in consideration.

**Chapter 5** Measurements and testing the validity of preliminary data analysis undertaken.

**Chapter 6** Conclusion.



# Contents

|                                               |            |
|-----------------------------------------------|------------|
| <b>Overview</b>                               | <b>iii</b> |
| <b>1 Introduction</b>                         | <b>1</b>   |
| 1.1 Neutrino Physics . . . . .                | 3          |
| 1.2 Neutrino detection . . . . .              | 4          |
| 1.2.1 Water cherenkov . . . . .               | 4          |
| 1.2.2 Neutron detection . . . . .             | 5          |
| <b>2 The ANNIE Experiment</b>                 | <b>7</b>   |
| 2.1 Physics of the experiment . . . . .       | 8          |
| 2.2 Neutrino beam . . . . .                   | 9          |
| 2.3 The Hall . . . . .                        | 12         |
| 2.3.1 Water tank . . . . .                    | 12         |
| 2.3.2 Photodetectors . . . . .                | 13         |
| 2.3.3 Veto and MRD . . . . .                  | 15         |
| <b>3 Data Acquisition</b>                     | <b>17</b>  |
| 3.1 Main DAQ Chain and VME Chain . . . . .    | 18         |
| 3.1.1 Hardware . . . . .                      | 18         |
| 3.1.2 Software . . . . .                      | 19         |
| 3.2 MRD Chain . . . . .                       | 21         |
| 3.2.1 Hardware . . . . .                      | 21         |
| 3.2.2 Software . . . . .                      | 22         |
| 3.3 Future improvement . . . . .              | 24         |
| <b>4 Data Analysis procedures</b>             | <b>27</b>  |
| 4.1 Individual pulse analysis . . . . .       | 27         |
| 4.2 Event definition . . . . .                | 28         |
| 4.3 Signal and noise discrimination . . . . . | 30         |
| 4.4 Data selection . . . . .                  | 30         |
| <b>5 Data analysis results</b>                | <b>33</b>  |
| 5.1 Cosmic background data . . . . .          | 33         |
| 5.2 Threshold dependence . . . . .            | 34         |
| 5.2.1 Voltage . . . . .                       | 35         |
| 5.2.2 PMTs fired . . . . .                    | 35         |
| 5.2.3 Rejection window . . . . .              | 35         |
| 5.3 Michel decay . . . . .                    | 35         |
| 5.4 Neutron yield . . . . .                   | 35         |
| 5.5 First MRD data . . . . .                  | 35         |
| <b>6 Conclusions</b>                          | <b>37</b>  |

|          |                                  |           |
|----------|----------------------------------|-----------|
| <b>A</b> | <b>Booster Neutrino Beam</b>     | <b>39</b> |
| A.1      | BNB details . . . . .            | 39        |
| A.2      | Resistive Wall Monitor . . . . . | 41        |
| <b>B</b> | <b>Employed CAMAC modules</b>    | <b>43</b> |
| B.1      | USB Camac Controller . . . . .   | 43        |
| B.2      | TDC . . . . .                    | 43        |
| B.3      | ADC . . . . .                    | 43        |

# Chapter 1

## Introduction

Just copied and pasted random stuff, eventually i'll have to clean this mess. Ignore it for now. Brief introduction here on SM and neutrinos maybe?

The Standard Model (SM) describes the strong, electromagnetic, and weak interactions of elementary particles in the framework of quantum field theory. It is a gauge theory based on the local symmetry group

$$\mathrm{SU}(3)_C \otimes \mathrm{SU}(2)_L \otimes \mathrm{U}(1)_Y \quad (1.1)$$

where  $C$ ,  $L$  and  $Y$  denote color, left-handed chirality and weak hypercharge, respectively. The gauge group uniquely determines the interactions and the number of vector gauge bosons that correspond to the generators of the group. They are eight massless gluons that mediate strong interactions, corresponding to the eight generators of  $\mathrm{SU}(3)_C$ , and four gauge bosons, of which three are massive ( $W^\pm$  and  $Z$ ) and one is massless, corresponding to the three generators of  $\mathrm{SU}(2)_L$  and one generator of  $\mathrm{U}(1)_Y$ , responsible for electroweak interactions. The electroweak part of the SM, based on the symmetry group  $\mathrm{SU}(2)_L \otimes \mathrm{U}(1)_Y$ , determines the interactions of neutrinos. In the SM, electroweak interactions can be studied separately from strong interactions, because the symmetry under the color group is unbroken and there is no mixing between the  $\mathrm{SU}(3)_C$  and the  $\mathrm{SU}(2)_L \otimes \mathrm{U}(1)_Y$  sectors. Electromagnetic and weak interactions must be treated together because there can be a mixing between the neutral gauge bosons of  $\mathrm{SU}(2)_L$  and  $\mathrm{U}(1)_Y$  [543]. As in all gauge theories, the symmetry group of the SM fixes the interactions, i.e. the number and properties of the vector gauge bosons, with only three independent unknown parameters, the three coupling constants of the  $\mathrm{SU}(3)_C$ ,  $\mathrm{SU}(2)_L$  and  $\mathrm{U}(1)_Y$  groups, all of which must be determined from experiments. On the other hand, the number and properties of scalar bosons and fermions are left unconstrained, except for the fact that they must transform in a definite way under the symmetry group, i.e. they must belong to the representations of the symmetry group, and the fermion representations must lead to the cancellation of quantum anomalies [31, 201, 268, 572, 517]. In the SM, the number of scalar bosons and fermions and their arrangement in the representations of the symmetry group are chosen in a heuristic way. The scalar bosons are chosen in order to implement, in a minimal way, the Higgs mechanism for the generation of masses, whereas the number and properties of fermions are determined by experiments. It is remarkable that all the known elementary fermions can be accommodated in appropriate representations of the symmetry group of the SM with exact cancellation of quantum anomalies. A puzzling feature of Nature is the existence of three generations of fermions with identical properties, except for different masses. This feature is unexplained in the SM. The known elementary fermions are divided in two categories, quarks and leptons [12], according to the scheme 1 st generation quarks: leptons: 2 nd generation 3 rd generation u (up), c (charm), t (top), d (down), s (strange), b (bottom); e (electron neutrino), (muon neutrino), (tau neutrino), e (electron), (muon),

(tau). They are distinguished by the fact that quarks participate in all the interactions (strong, electromagnetic, weak, and gravitational), whereas leptons participate in all the interactions except strong interactions. The masses and electric charges of quarks and leptons are given in Tables 3.1 and 3.2. The corresponding antiparticles have the same mass and opposite electric charge. All fundamental fermions have spin 1/2.

A neutrino is a chargless lepton, therefore it is a fermion which interacts only via the weakforce.

The predictions of the existence of the W and Z bosons, the gluon, the top and charm quarks made the fortune of the Standard Model (SM). Their redicted properties were experimentally confirmed with good precision and the recent discovery of the Higgs Boson [? ] [? ] is the last crowning achievement of SM.

Despite being the most successful theory of particle physics to date, the Standard Model is actually limited in its approximation to reality, in that some clear evidences cannot be explained. The most outstanding discovery is the neutrino oscillations, which has proved that the neutrinos are not all massless, as it is assumed by theory. Mass terms for the neutrinos can be included in the SM, with the implications of theoretical problems. Likewise, the SM is unable to provide an explanation of the observed asymmetry between matter and anti-matter. It was noted by Sakharov [? ] that a solution to this puzzle would require some form of C and CP violation in the early Universe, along with Baryon number violation and out-of-equilibrium interactions. These facts suggest that the Standard Model is not a complete theory and additional physics Beyond the Standard Model (BSM) is required.

Even though evidence of CP-violation has been found in hadron physics !danielscullyintroduction!, this does not suffice for the asymmetry required to explain cosmological observations. M. Fukugita and T. Yaganida pointed out an elegant mechanism to generate the baryon excess from lepton asymmetries. This process is referred as Leptogenesis and necessitates a Standard Model extension, such as the introduction of right-handed neutrinos, permitting implementation of the see-saw mechanism and providing the neutrinos with mass. On the other hand, the extended model is able to spontaneously generate leptons from the decays of right-handed neutrinos. Eventually, the lepton asymmetry is converted to baryon asymmetry by sphalerons. This process is referred as Leptogenesis and involves Majorana mass terms and the seesaw may transform into the baryon number excess through the unsuppressed baryon number wolutlon of electroweak processes at high temperatures

Once again the discovery of neutrino oscillations could hold the answer since the phenomenon also allows for the possibility of leptonic CP-violation. Various mechanisms have been proposed that would allow CP-violation in the lepton sector to provide the necessary asymmetry in the baryons [5]. Establishing whether or not CP-violation does occur in neutrinos is therefore a priority.

It is clear that the study of neutrinos is of vital importance to the future development of particle physics, in particular through the study of oscillations. However, as will be discussed in Chapter 2, precision measurements of neutrino oscillations are predicated on improving our understanding of neutrino-nucleus interactions.

There are multiple channels through which neutrinos can interact with nuclei and, as described in Chapter 3, many of them are in need of improvements in both our experimental and theoretical understanding. In Chapter 4 one interaction channel, coherent pion production, is identified as being of particular importance to the field, in need of experimental input, and with the potential for significant improvements in the near future. The T2K neutrino oscillation experiment, described in Chapter 5, provided an opportunity to contribute to this field, the results of which are reported in Chapter 6.

The neutrino was postulated first by Wolfgang Pauli in 1930 to explain how beta decay

could conserve energy, momentum, and angular momentum (spin). In contrast to Niels Bohr, who proposed a statistical version of the conservation laws to explain the event, Pauli hypothesized an undetected particle that he called a “neutron”, using the same -on ending employed for naming both the proton and the electron. He considered that the new particle was emitted from the nucleus together with the electron or beta particle in the process of beta decay.[8][nb 2]

In Fermi’s theory of beta decay, Chadwick’s large neutral particle could decay to a proton, electron, and the smaller neutral particle (flavored as an electron antineutrino):

Fermi’s paper, written in 1934, unified Pauli’s neutrino with Paul Dirac’s positron and Werner Heisenberg’s neutron–proton model and gave a solid theoretical basis for future experimental work. However, the journal Nature rejected Fermi’s paper, saying that the theory was “too remote from reality”. He submitted the paper to an Italian journal, which accepted it, but the general lack of interest in his theory at that early date caused him to switch to experimental physics.[10]:24[11]

Nevertheless, even in 1934 there were hints that Bohr’s idea — that the energy conservation laws were not followed — was incorrect. At the Solvay conference of 1934, the first measurements of the energy spectra of beta decay were reported, and these spectra were found to impose a strict limit on the energy of electrons from each type of beta decay. Such a limit was not expected if the conservation of energy was not upheld, in which case any amount of energy would be expected to be statistically available in at least a few decays. The natural explanation of the beta decay spectrum as first measured in 1934 was that only a limited (and conserved) amount of energy was available, and a new particle was sometimes taking a varying fraction of this limited energy, leaving the rest for the beta particle. Pauli made use of the occasion to publicly emphasize that the still-undetected “neutrino” must be an actual particle.

The idea of neutrino was put forward by W. Pauli in 1930. This was a dramatic time in physics. After it was established in the Ellis and Wooster experiment that the average energy of the electrons produced in the beta-decay is significantly smaller than the total released energy, only the existence of neutrino, a neutral particle with a small mass and a large penetration length (much larger then the penetration length of the photon), which is emitted in the  $\beta$ -decay together with the electron, could save the fundamental law of the conservation of energy. At the time when the neutrino hypothesis was proposed the only known elementary particles were electron and proton. In this sense neutrino (more exactly electron neutrino) is one of the “oldest” elementary particles. However, the existence of the neutrino was established only in the middle of the fifties when neutron, muon, pions, kaons,  $\Lambda$  and other strange particles were discovered. We know at present that the twelve fundamental fermions exist in nature: six quarks u, d, c, s, t, b, three charged leptons e,  $\mu$ ,  $\tau$  and three neutrinos  $\nu_e$ ,  $\nu_\mu$ ,  $\nu_\tau$ . They are grouped in the three families, which differ in masses of particles but have universal electroweak interaction with photons and vector  $W^\pm$ , Z bosons. In the Lagrangian of the electroweak interaction, neutrinos enter on the same footings as the quarks and charged leptons. In spite of this similarity of the electroweak interaction neutrinos are special particles.

## 1.1 Neutrino Physics

**Neutrino physics, like wak interactions.** There are two basic differences between neutrinos and other fundamental fermions.

- At all available at present energies, cross section of the interaction of neutrinos with matter is many order of magnitude smaller than the cross section of the electromagnetic interaction of leptons with matter (via the exchange of the virtual photon).

This is connected with the fact that neutrinos interact with matter via the exchange of the heavy virtual  $W^\pm$  and  $Z$  bosons.

- Neutrino masses are many orders of magnitude smaller than the masses of leptons and quarks. Because of the extreme smallness of the neutrino cross section, special methods of the detection of neutrino processes must be developed.

The Physics of neutrino-nucleus interactions is strictly influenced by the complex interplay of multiple particles and current models are limited in their approximation to reality. As more neutrino data become available, lack of knowledge of the fine details of the interactions begins to narrow the reach of future experiments. Under these circumstances, experiments that observe neutrino-nucleus interactions using different techniques are essential to develop more accurate models that allow an era of precision physics in neutrino experiments. A key handle in understanding neutrino-nucleus interaction is the number and type of nucleons ejected from the interaction, which are a valuable constraint on theoretical models.

One example is the first double differential cross section for charged-current quasi-elastic (CCQE) interactions, published by the MiniBooNE experiment [ref]. It has been shown that these and other data are finely described by models including two-body currents, where low-energy neutrinos scatter off correlated pairs of nucleons. A relevant predicted consequence of two-body currents is higher multiplicity of final-state nucleons, indeed.

## 1.2 Neutrino detection

LAr?

### 1.2.1 Water cherenkov

As a charged particle travels, it disrupts the local electromagnetic field in its medium. In particular, the medium becomes electrically polarized by the particle's electric field. If the particle travels slowly then the disturbance elastically relaxes back to mechanical equilibrium as the particle passes. When the particle is traveling fast enough, however, the limited response speed of the medium means that a disturbance is left in the wake of the particle, and the energy contained in this disturbance radiates as a coherent shockwave.

“Ring-imaging” Cherenkov detectors take advantage of a phenomenon called Cherenkov light. Cherenkov radiation is produced whenever charged particles such as electrons or muons are moving through a given detector medium somewhat faster than the speed of light in that medium. In a Cherenkov detector, a large volume of clear material such as water or ice is surrounded by light-sensitive photomultiplier tubes. A charged lepton produced with sufficient energy and moving through such a detector does travel somewhat faster than the speed of light in the detector medium (although somewhat slower than the speed of light in a vacuum). The charged lepton generates a visible “optical shockwave” of Cherenkov radiation. This radiation is detected by the photomultiplier tubes and shows up as a characteristic ring-like pattern of activity in the array of photomultiplier tubes. As neutrinos can interact with atomic nuclei to produce charged leptons which emit Cherenkov radiation, this pattern can be used to infer direction, energy, and (sometimes) flavor information about incident neutrinos.

$$\frac{E}{m_0 c^2} > \frac{1}{\sqrt{1 - 1/n^2}} \quad (1.2)$$

### 1.2.2 Neutron detection

The Super-Kamiokande (SK) [1] is the largest light water Cherenkov detector that has been successfully observing solar, atmospheric and accelerator neutrinos. Recently the addition of 0.2 % of a water soluble gadolinium (Gd) compound to SK has been proposed [2]. This modification can greatly improve the detection sensitivity of anti-electron neutrinos. The inverse beta interaction in the water, emits a positron and a neutron. The positron, radiating Cherenkov photons, is immediately detected. The neutron is quickly thermalized in the water, and is then captured by Gd with a probability of 90 %. Upon capturing a neutron the Gd emits 3-4 gamma rays having a total energy of about 8 MeV. The time and spatial correlation of the positron and neutron capture events (20 us and 4 cm) can significantly reduce the backgrounds, and hence enhance the nu e signal events.



## Chapter 2

# The ANNIE Experiment

As more neutrino data become available, lack of knowledge of the fine details of the neutrino-nucleus interactions begins to limit the physics reach of future experiments. For instance, final-state neutron abundance from pure neutrino interactions are currently poorly known and difficult to measure. Data on neutron yield in relation to energy and direction of final-state muons can be used to better constrain nuclear models of neutrino interaction physics and are an essential input to Monte Carlo models, used for calculating detection efficiencies, expected background rates, accurate limits, and confidence levels. The count of neutrons can also be used to reject contamination by atmospheric neutrino interactions in proton decay experiments and in a sample of diffuse supernova background neutrinos and may also help to statistically address wrong-sign contamination in oscillation analyses. In addition to helping understand fundamental neutrino-interaction physics, tagging events by the presence and number of final-state neutrons can provide physics analyses with a better handle for signal/background separation and even allow for discrimination between different types of neutrino interactions.



**Figure 2.1:** Logo of the ANNIE experiment.

A study on final-state neutron abundance can be accomplished by the **Accelerator Neutrino Neutron Interaction Experiment** (ANNIE), which will provide a complementary measurement of neutron yields in neutrino-nucleon interactions. The ANNIE experiment is a prototype neutrino detector currently taking data at the Fermi National Accelerator Laboratory (FNAL, Fermilab), in Chicago, USA. It consists of a small water Cherenkov detector, placed at

the former location of the SciBooNE experiment ref[Phys. Rev. D 78 (2008) 112004] and deployed on the intense Booster Neutrino Beam (BNB). An upstream forward Veto and a downstream Muon Range Detector (MRD) are also installed in the hall. The experiment aims to be a test bed for many new technologies, as the gadolinium-doped water and the use of early prototype Large Area Picosecond Photodetectors (LAPPDs). Neutron tagging in Gd-loaded water may play a significant role in reducing backgrounds from atmospheric neutrinos in next generation proton-decay searches using megaton-scale Water Cherenkov detectors, like Hyper-Kamiokande ref. Similar techniques might also be useful in the detection of supernova neutrinos. Accurate determination of neutron tagging efficiencies will require a detailed understanding of the number of neutrons produced by neutrino interactions in water as a function of momentum transferred. This accuracy can be achieved by using precision timing, thank to the LAPPDs, to localise interaction vertices in the small fiducial volume of the detector. The ANNIE experiment will be an innovative application

of these devices demonstrating their feasibility for Water Cherenkov neutrino detectors.

The experiment is planned to proceed in two stages, spread over five years:

**Phase I** a partially-instrumented test-beam run using only Photomultipliers (PMTs) for the purpose of measuring critical neutron backgrounds to the experiment;

**Phase II** a longer run with a more fully-instrumented detector where incremental research and development for the LAPPDs and accompanying fast electronics will be fulfilled, as long as the expansion of the photodetector coverage (both LAPPDs and PMTs) required.

*Year 1* will focus on the R&D, particularly on the development of the Data Acquisition system, along with the testing in water of the first model of LAPPD. Installation of the first LAPPDs and a significant fraction of the additional PMTs, as well as the calibration system, will take place in *Year 2*. Data-taking would commence in *Year 3* and continue through *Year 5*, with the physics reach of the detector improving as the fraction of LAPPDs increases over time. Publication of derived results would occur by the end of *Year 5*.

This thesis takes place at the beginning of *Year 1*, where testing of the Phase I experimental setup is tested and R%D is undertaken.

## 2.1 Physics of the experiment

As established previously, detection of final state neutrons from nuclear interactions would have a transformative impact on a wide variety of neutrino physics measurements. Nevertheless there are major limitations on the effective execution of neutron tagging techniques, for both sides of Physics:

- theoretically, large theoretical uncertainties on the nuclear mechanisms that produce neutrons in GeV-scale neutrino interactions are not still clear;
- experimentally, the neutron yield hasn't been satisfactorily measured yet.

The physics of neutrino-nucleus interactions depends on the complex interplay of multiple particles and different energy scales, and it can vary greatly among target materials. It is also known that the number and type of nucleons ejected from the interaction provides a valuable constraint on models of neutrino-nucleus interactions. ANNIE can study neutron yields from mostly-pure neutrino interactions separately and will study neutron yields in relation to the energy and direction of final-state muons with respect to the original neutrino.

The principal process to be considered at the first order is the charged current (CC) exchange, which yields a proton (neutron) from the neutrino (anti-neutrino) interaction, and neutral current (NC) interactions, which produce either protons or neutrons. Higher-order processes and multi-scale nuclear physics, including secondary (p,n) scattering of struck nucleons within the nucleus, charge exchange reactions of energetic hadrons in the nucleus (e.g.,  $\pi^- p \rightarrow n \pi^0$ ), and Meson Exchange Currents (MEC), where the neutrino interacts with a correlated pair of nucleons, all modify these expectations. The theory describing these interactions is under development and is often weakly constrained by the available data. One of the main results published by the MiniBooNE collaboration ref, concerns the Charged Current Quasi-Elastic interactions.

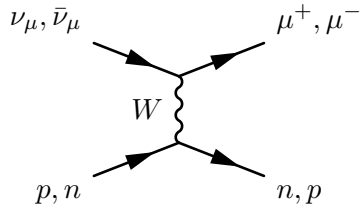


**Figure 2.2:** CC interaction of a neutrino with a nucleon, producing the corresponding lepton. This interaction is called Quasi Elastic.

The first double differential cross section for CCQE interactions are better described by models including two-body currents, where low-energy neutrinos scatter off correlated pairs of nucleons. A relevant predicted consequence of two-body currents is higher multiplicity of final-state A key handle in understanding neutrino-nucleus interaction is the number and type of nucleons ejected from the interaction. [More on this. Ask Teppei?](#)

The search for a delayed signal from neutron capture on Gadolinium (Gd) salts dissolved in water is a promising technique for detecting final state neutrons.

It is therefore critical that we experimentally characterise the probability of producing zero ( $P(N=0)$ ), one ( $P(N=1)$ ), or multiple ( $P(N>1)$ ) neutrons from a neutrino interaction, as a function of both interaction type and momentum transfer. Even moderately energetic neutrons ranging from tens to hundreds of MeV will quickly lose energy by collisions with free protons and oxygen nuclei in water. Once thermalised, the neutrons undergo radiative capture, combining with a nearby nucleus to produce a more tightly bound final state, with excess energy released in a gamma-ray ( ) cascade. Gd-doped water enhances the capture cross-section compared to pure water (49,000 barns compared with 0.3 barns on a free proton) and, since the cascade happens at higher energies (8 MeV vs 2.2 MeV), it produces enough optical light to be reliably detected in a large target volume.

ANNIE will require collecting data from sufficient neutrino interactions to make accurate statements about neutron yield in an inclusive sample of neutrino interactions. The primary goal is to measure distributions of neutron yield from muon neutrino charged current interactions versus various kinematic observables such as momentum transfer. It is expected that this would require on the order of 10K neutrino interactions considering the efficiencies and acceptances of the experimental setup ( $\sim 10\%$  of the interactions in the detector). This corresponds to one year of data. With additional statistics (additional 2 years of data) and improved detector performance, the more demanding goal of studying neutron yields for specific event classes can be met.

[What can happen inside the tank? Cosmic, beam and stuff, what they triggers, how they can be seen, how the detectors react.](#)

## 2.2 Neutrino beam

ANNIE is run on axis from the *Booster Neutrino Beam* (BNB), which deploys 8.89 GeV protons accelerated from the Fermilab booster operating at 15 Hz. The primary beam from the *Linac* uses protons accelerated to 8 GeV kinetic energy by the Fermilab booster. Selected batches containing approximately  $5 \times 10^{12}$  protons are extracted and bent toward a beryllium target via dipole magnets. Each spill is composed of 81 bunches of protons, approximately 6 ns wide each and 19 ns apart, for a total spill duration of 1.6  $\mu$ s. As far as the detector is concerned, the neutrino beam is seen to arrive with a spill frequency of 15 Hz, divided in pulse train, around 1 s apart each other.

Beam proton trajectories and positions are monitored on a pulse-by-pulse basis. Upstream of the target, the primary proton beam is monitored on a pulse-by-pulse basis using four systems: two toroids measuring its intensity (protons-per-pulse), beam position monitors (BPM) and a multi-wire chamber determining the beam width and position, and a resistive wall monitor (RWM) measuring both the time and intensity of the beam spills. A logic signal is also generated by the last device for every intensity peak. It is employed to trigger the experiment in correspondence of each spill. The BNB is dealt in detail in the appendix B.

Hadronic interactions of the protons with the target material produce a beam of secondary mesons, mostly pions and kaons. A magnetic focusing horn, shown in Fig. 2.3, surrounds the beryllium target, bending and sign-selecting the secondary particles emitted along the direction pointing to the hall. The focusing is produced by the toroidal mag-

netic field present in the air volume between the horn's two coaxial conductors made of aluminium alloy. The beam of focused, secondary mesons emerging from the target/horn region is further collimated, via passive shielding, and allowed to decay into neutrinos in a cylindrical decay region filled with air at atmospheric pressure, 50 m long and 90 cm in radius.

The polarity of the horn current flow can be (and has been) switched, in order to focus negatively charged mesons, and therefore produce an antineutrino instead of a neutrino beam. The  $\pi^\pm$  mesons have a mass of 139.6 MeV and a mean lifetime of  $2.6 \times 10^{-8}$  s. The primary decay mode of a pion, with a branching fraction of 99.9877 %, is a leptonic decay into a muon and a muon neutrino:

$$\pi^+ \rightarrow \mu^+ \nu_\mu \quad (2.1)$$

$$\pi^- \rightarrow \mu^- \bar{\nu}_\mu \quad (2.2)$$

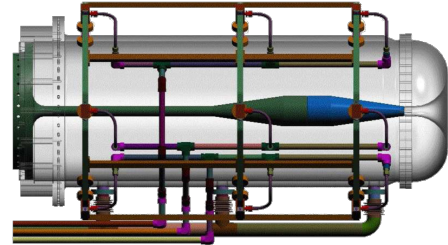
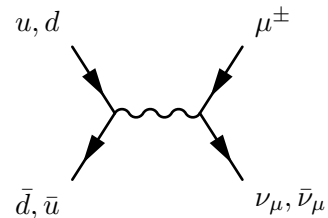


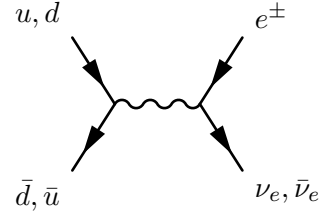
**Figure 2.3:** BNB horn system.



The second most common decay mode of a pion, with a branching fraction of 0.0123 %, is also a leptonic decay into an electron and the corresponding electron antineutrino:

$$\pi^+ \rightarrow e^+ \nu_e \quad (2.3)$$

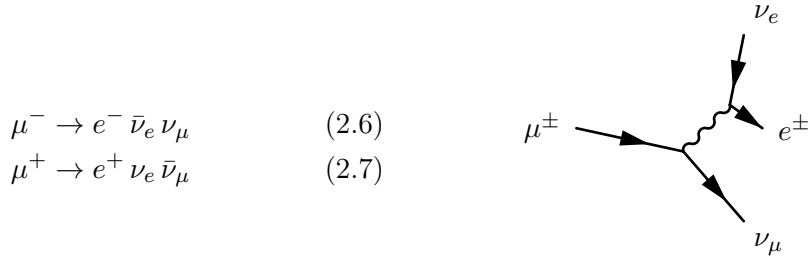
$$\pi^- \rightarrow e^- \bar{\nu}_e \quad (2.4)$$



In spite of the considerable differences in the space momentum, the suppression of the electronic decay mode with respect to the muonic one is a well known effect, called *helicity suppression*: due to the great mass of the muon ( $m_\mu = 105.658$  MeV) compared to the electron ( $m_e = 0.510$  MeV), the helicity-chirality correspondence is stronger for the latter. Given that the  $\pi$  mesons are spinless, neutrinos are left-handed, and antineutrinos are right-handed, the muonic channel is preferred because of spin and linear momentum preservation. The suppression of the electronic decay mode with respect to the muonic one is given approximately within radiative corrections by the ratio:

$$R_\pi = \left( \frac{m_e}{m_\mu} \right)^2 \left( \frac{m_\pi^2 - m_e^2}{m_\pi^2 - m_\mu^2} \right) = 1.283 \times 10^{-4} \quad (2.5)$$

**Have to add something about muon decay here.** Neutrinos are also produced by muons' decay. Muons are unstable elementary particles and decay via the weak interaction. The dominant decay mode, called *Michel decay*, is also the simplest possible: because lepton numbers must be conserved, one of the product neutrinos of muon decay must be a muonic neutrino and the other an electronic antineutrino, along with an electron, because of the charge preservation. Vice versa, an antimuon decay produces the corresponding antiparticles. These two decays are:



The mean lifetime of the muon is  $(2.196,981,1 \pm 0.000,002,2) \mu\text{s}$ .

A beam absorber located at the end of the decay region stops the hadronic and muonic component of the beam, and only an almost pure neutrino beam pointing towards the detector remains.

**From SciBooNE - charged current etc.** Neutrino flux predictions are the same produced by the SciBooNE collaboration, obtained via a GEANT4-based beam Monte Carlo simulation. The same simulation code developed by the MiniBooNE Collaboration is used [24], where a realistic description of the geometry and materials present in the BNB target hall and decay region is used. Primary protons are generated according to the expected beam optics properties upstream of the target. The interactions of primary protons with the beryllium target are simulated according to state-of-the-art hadron interaction data. Of particular importance for this analysis is a  $\pi^+$  production in proton-beryllium interactions, which uses experimental input from the HARP [25] and BNL E910 [26] experiments. Production of secondary protons, neutrons, charged pions, and charged and neutral kaons is taken into account, and elastic and quasi-elastic scattering of protons in the target are also simulated. Particles emanating from the primary proton-beryllium interaction in the target are then propagated within the GEANT4 framework, which accounts for all relevant physics processes. Given the importance of the target (beryllium and aluminium) hadronic reactions, these are described by custom models, while other hadronic processes and all electromagnetic processes (energy loss, multiple scattering, effect of horn magnetic field, etc.) are described according to default GEANT4 physics lists.

A second, FORTRAN-based Monte Carlo code is responsible for generating the neutrino kinematics distributions from meson and muon decays, and for obtaining the final neutrino fluxes extrapolated to the detector hall with negligible beam Monte Carlo statistical errors. Once produced by the simulation, neutrinos are extrapolated along straight lines toward the detector and all neutrinos whose traces cross any part of the active volume are considered for the flux predictions. Based on accurate survey data, the distance between the centre of the beryllium target and the centre of the SciBar detector is taken to be 99.9 m, with the detector located on beam axis within a tolerance of a few centimetres.

The neutrino flux prediction at the detector location and as a function of neutrino energy is shown in Fig. 2.4. A total neutrino flux per proton on target of  $2.2 \times 10^{-8} \text{ cm}^{-2}$  is expected at the hall location and in neutrino running mode (positive horn polarity), with a mean neutrino energy of 0.7 GeV. The flux is dominated by muon neutrinos (93 % of total), with small contributions from muon antineutrinos (6.4 %), and electron neutrinos and antineutrinos (0.6 % in total). For the neutrino flux predictions, no information from

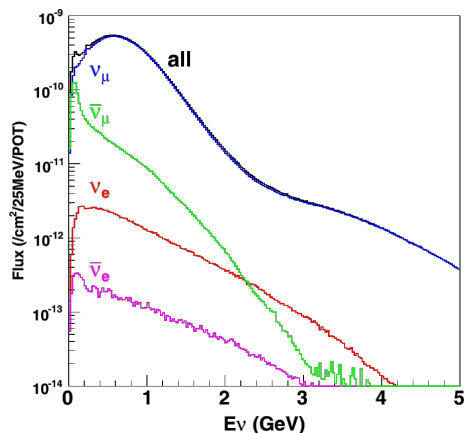


**Figure 2.4:** Neutrino flux predictions from the GEANT4/FORTRAN simulation.

BNB (SciBooNE or MiniBooNE) neutrino data was used as experimental input. The *projected number of protons* incident on the target (POT) per year for the BNB is about  $2 \times 10^{20}$  POT. The rates expected per year when running in neutrino mode for one ton of water (see section ref) are about sixteen thousands neutrino interactions, where eleven thousands of those would be  $\nu_\mu$  CC interactions. This spectrum peaks ideally in the region of interest at 700 MeV as a result of the simulation shown in Fig. 2.4, and has the target rate of neutrino interactions per year. Another consideration beyond the rates and spectra of in-detector neutrino interactions is the probability of seeing multiple events in one beam spill. The number of muon neutrino per spill at the SciBooNE location is found to be significantly less than one. In fact from the preliminary simulations, the neutrino interactions occur in the tank approximately every 150 spills of  $4 \times 10^{12}$  POTs. Additionally our simulations suggest an externally generated muon enters the tank once every  $\sim 195$  spills. These rates are ideal as they ensure single neutrino interactions in the detector.

## 2.3 The Hall

The experiment is set up in the former site of the SciBooNE experiment refagain?, located 8 m below the surface and the 100 m from the BNB target. Already existing instrumentation in the hall is borrowed by the ANNIE experiment.

### 2.3.1 Water tank

The main component of the experiment is the water tank, built and installed in the hall. It consists of a welded steel water tank, which dimensions are 10 ft (slightly more than three metres) of diameter per 13 ft (nearly four metres) of height, enclosing roughly 23 tonnes of water. The characteristic dimension of the tank can be compared to the diagonal of the cylinder, which is about five meters. It corresponds to circa seventeen light-nanoseconds. The inner volume is lined with a black, water tight plastic bag and outfitted with a PVC inner support structure mounted with 60 PMTs, and capable of ultimately housing several hundred photo-sensors. The tank is filled with pure water and used in conjunction with a smaller acrylic vessel containing Gd-loaded scintillator to measure neutron backgrounds, called Neutron Volume Capture (NCV). Due to its two orders of magnitude smaller volume compared to Super-Kamiokande, ANNIE's water transparency requirements are less stringent: ANNIE needs only to keep a transparency about 25 meters to lose less than 10 % of the light, as opposed to SK's effective water attenuation length of 90 meters. The ANNIE water volume requires a source of dry nitrogen in order to suppress the growth of biologics in the water. This nitrogen is bubbled through the water during fill and afterwards a blanket of nitrogen will be maintained above the surface of the water. The re-circulation is kept as low as necessary to maintain a pure N<sub>2</sub> environment. ANNIE also relies on the plastic liner to prevent ions, that might compromise transparency, from leaching into the water from the tank walls. Water quality is supposed to be monitored using the detected light intensity from cosmic ray muons.

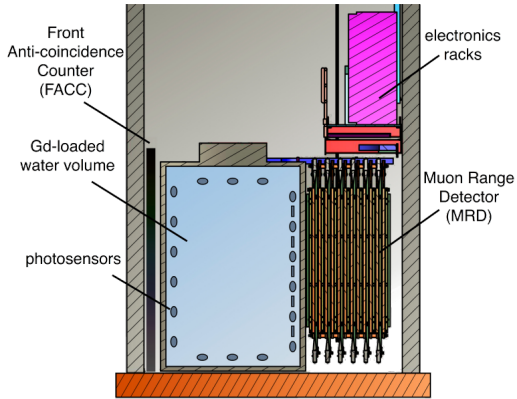


**Figure 2.5:** Schematic of the experimental hall.

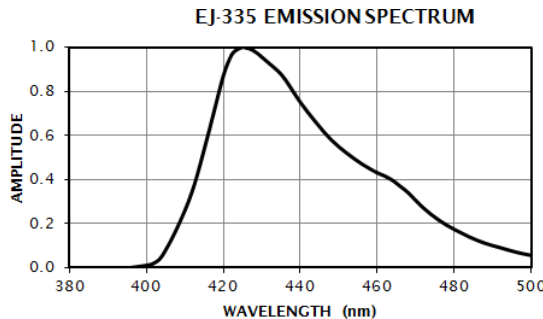


**Figure 2.7:** EJ-335 emission spectrum. This scintillator contains mineral oil substituted for some of the aromatic solvent for purposes of higher hydrogen content and higher flash point for use in very large tanks. The gadolinium content is 0.25% by weight. The wavelength of peak emission is 424 nm.



**Figure 2.6:** Design of the NCV.

A concentrated solution of high-quality (99.99% TREO<sup>1</sup>) gadolinium sulphate  $\text{Gd}_2(\text{SO}_4)_3$  will be mixed in a portable polypropylene barrel with pure water. The available 50 kg of Gd are enough for one test loading (4 kg) and one full loading (40 kg), with 6 kg left over for various other studies and tests. Thanks to the complex of water re-circulation system, the Gd-loaded water can be removed and stored in a secondary tank, then returned and re-purified with minimal loss of Gd, between ANNIE's runs. Upon completion of the experiment the gadolinium can be easily recovered using a portable demineraliser. Measurement of neutron background will be possible thanks to the NCV. It consists of a moveable 2.5 cm thick, 50 cm×50 cm transparent acrylic

vessel, which holds 100 L of Gd-doped EJ-335 liquid scintillator, specialised for neutron detection. The light spectrum is shown in Fig. 2.7.

The vessel is weighted so as to have a negative buoyancy. Position dependence of the neutron rates from different overburdens of water can be studied by raising and lowering the NCV and translating it along the beam axis.

### 2.3.2 Photodetectors

The core of the experiment is the Cherenkov light detection. The coverage provided by 60 8" PMTs borrowed from the WATCHBOY experiment<sup>2</sup> is enough for the Phase I. The photomultipliers are mounted in a frame on the bottom of the tank, facing upward. The frame is designed to support both the weight of the phototubes in gravity as well as the buoyant forces in water.

As noted earlier, the necessary photo-coverage to reconstruct events in water will be achieved in ANNIE Phase II by:

- reusing the 8" Hamamatsu PMTs recovered from ANNIE Phase I.

<sup>1</sup>TREO expresses the Total Rare Earth Oxide percentage in the element.

<sup>2</sup>The WATCHBOY experiment was designed to measure the rate of radionuclide production in water created by muon spallation. Three primary nuclei of interest, <sup>11</sup>Li, <sup>8</sup>He, and <sup>9</sup>Li, can produce a high energy beta particle in coincidence with a neutron, thus mimicking an antineutrino induced inverse beta decay. The experiment was constructed in 2013 at the Kimballton Underground Research Facility (KURF) in Virginia, US.

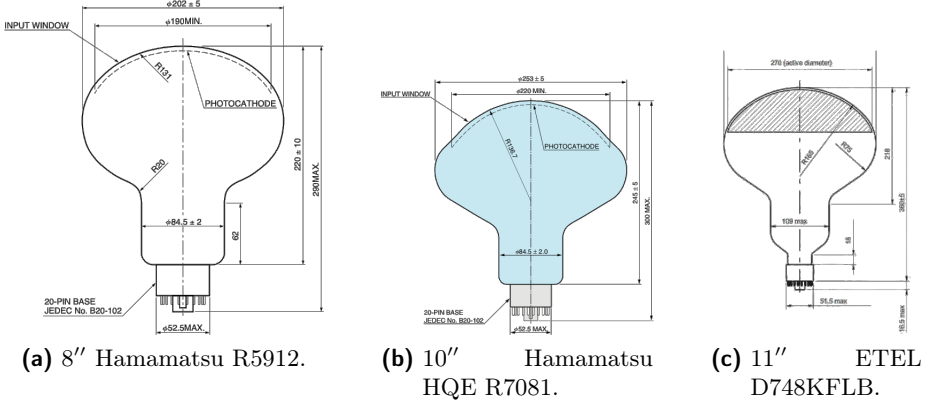


**Figure 2.8:** Schematic of the PMTs employed in the experiment.

- purchasing new High Quantum Efficiency (HQE) 10'' Hamamatsu PMTs;
- employing refurbished 11'' Electron Tubes Enterprise PMTs [arXiv:1512.06916v2].

In order to determine the necessary photocathode coverage, a series of simulations has been run with different sizes and numbers of PMTs. These full simulations consider neutron captures on both Gd (90 %) and the hydrogen from the water (10 %). After cost and availability are taken into account, it is found that the detection can be optimised by using 58 8'' tubes, 20 11'' tubes, and 45 HQE 10'' tubes. Detection probability depends on the number of PMTs hit per neutron capture. Gadolinium captures typically produce several photons, therefore the probability of observing enough hits to detect the event is related to the number of photoelectrons produced. This number is strictly correlated with the number of hits. The predictions agree well with a simple scaling argument based on measurements at Super-Kamiokande. Using the planned mix of 11'' tubes, 8'' tubes, and HQE 10'' tubes, it is found that 5 (good correlation) and 10 (strong correlation) photoelectrons are produced respectively 99 % and 94 % of the time.

**Have to improve LAPPDs section, but how much?** Precise vertex reconstruction will be required for the next stages of the experiment. In addition to the PMT coverage improvement, the use of advanced, high resolution photodetectors could have a transformative impact on future neutrino detectors relying on light collection. The most promising technology, selected for ANNIE, is the Large Area Picosecond Photodetector (LAPPD), a microchannel plate (MCP) based photomultiplier. It can achieve single photoelectron time resolutions less than 100 ps and spatial imaging capabilities to within a single centimetre. This provides a much crisper detection of the Cherenkov ring edge and greatly improves the ability to distinguish between closely separate rings. On the other hand, conventional PMTs have time resolution of the order of the nanosecond and act as a single pixel, despite the large active area. The combination of LAPPDs and PMTs allows the detector to work as a tracking detector, with track and vertex reconstruction approaching size scales of just a few centimetres. It also favours the reconstruction of events very close to the wall of the detector, thanks to the small thickness of the LAPPDs (less than 1.5 cm). The fiducial volume is thus maximised. The LAPPD capabilities also translate into better energy resolution and better discrimination between dark noise and photons from neutron captures.

I should put this in “physics of experiment” section. The maximum transit time for direct light to travel in the ANNIE tank is less than 20 ns. The difference in transit time between two photons arriving at the same photosensor from two different forward-pointing tracks is just a few nanoseconds. This is illustrated in Fig 6. For one LAPPD at the centre of overlapping Cherenkov rings, the time separation between photons from a muon and a

pion is less than a nanosecond. Time resolutions of 100 and 300 picoseconds are sufficient to resolve that separation. That time separation would be even larger at the photon hits further away from the overlap region. As time resolutions approach the nanosecond scale, typical of conventional PMTs, causal differences between the tracks get significantly washed out. Time resolution, however, is not the only essential characteristic. Spatial granularity and short single-PE detector response are also critical. Much of the information embedded in overlapping Cherenkov rings can only be extracted if each individual photon is measured independently. Conventional large area PMTs are single anode detectors. Moreover the rise times of PMT pulses are comparable to the time differences between the photons being measured. LAPPDs have a fine-grained 30 stripline anode and a single PE response with a rise time of a few hundred picoseconds. Large Monte Carlo ensembles show that photon pileup on LAPPDs is low enough that we typically see only one or two hits per channel. Thus, each photon can individually be measured. Our preliminary studies show that 20 LAPPDs can provide sufficient coverage and have well-suited performance characteristics for addressing the challenges of WCh reconstruction in a small volume. Better reconstruction could be possible as larger numbers of LAPPDs become available. Reaching a 10 % isotropic coverage would allow not only from identifying multi-track events but in also identifying the constituent particles and the exact topology potentially expanding the physics reach of the experiment.

### 2.3.3 Veto system and Muon Range Detector

mostly ok, I guess I have every information.

ANNIE is composed of two more detectors other than the water tank in the hall: the Veto system and a muon detector.

The Veto is provided by a Forward Anti-Coincidence Counter (FACC) consisting of two layers of overlapping scintillating paddles. Each layer employs 13 paddles to detect charged particles produced in the dirt upstream of the hall or muons from the BNB, which hasn't decayed. This allows the rejection of events in the tank unrelated to neutrino interactions. It employs 2" PMTs to read the signals from the scintillator.

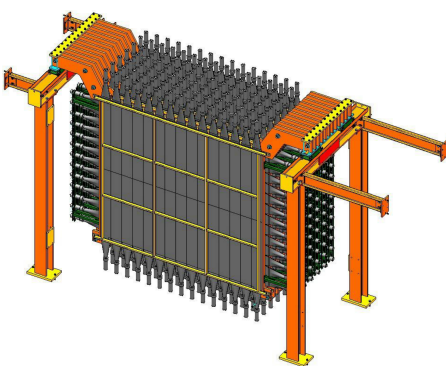


**Figure 2.9:** Drawing of the MRD.

An iron-scintillator sandwich, inherited from the SciBooNE experiment, is also in the hall. The Muon Range Detector (MRD) is used to range out and fit the direction of daughter muons produced by CCQE interactions in the water target. Its schematic drawing is shown in Fig. 2.9. The muon's energy can be reconstructed thus giving also a handle on the neutrino energy. The MRD is designed to measure the momentum of muons up to 1.2 GeV/c using the range measurement. It consists of 12 iron plates and 13 alternating horizontal and vertical scintillator planes. Each iron

plate is 5 cm thick, and covers an area of  $274 \times 305 \text{ cm}^2$ . The total mass of absorber material is approximately 48 tonnes, while the detector weighs about sixty tonnes. The density of a spare iron plate has been measured at several positions of the plate, to be  $7.841 \pm 0.002 \text{ g/cm}^3$ . Each scintillator plane consists of 20 cm wide, 6 mm thick scintillator paddles, as illustrated in Fig. 2.10. Each vertical plane is comprised of 138 cm long paddles, arranged in a  $2 \times 15$  array to have an active area of  $276 \times 300 \text{ cm}^2$ . On the other hand, each horizontal scintillator plane consists of 155 cm long paddles, arranged in a  $13 \times 2$  array to have an active area of  $260 \times 310 \text{ cm}^2$ . In total, 362 paddles, 182 vertical and

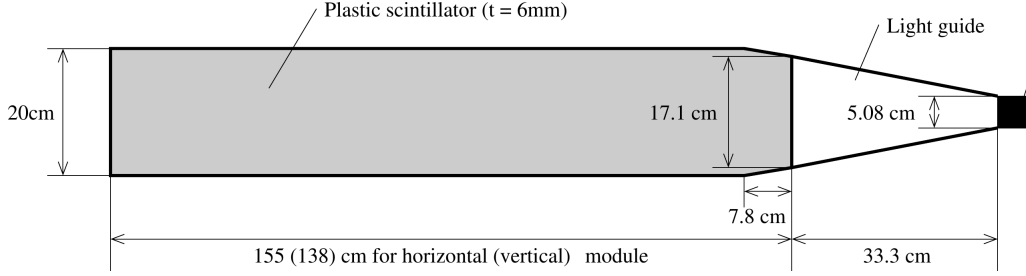


**Figure 2.10:** Paddle used for the MRD.

180 horizontal, are used in the MRD. The scintillator paddles are read out by five types of 2" PMTs; the vertical planes consist of Hamamatsu 2154-05 and RCA 6342A PMTs, the horizontal planes consist of EMI 9954KB, EMI 9839b and 9939b PMTs. All PMTs used for horizontal modules have 14 stage dynodes, while those used for vertical modules have 10 stage dynodes. This choice is due to space limitations. Hence, the PMTs used for the vertical planes have relatively low gain and efficiency compared to that used for horizontal planes. To ensure the same efficiencies, the vertical modules are amplified by the factor of 10 using LeCroy 612 amplifiers.

As far as the electronics are concerned, the FACC and MRD are essentially the same system. Both detectors are composed of scintillating paddles and small phototubes, and both detectors follow the same rectilinear geometry. The FACC consists of two layers of 13 horizontal paddles. On the MRD side, only a fraction of the detector is operational for Phase I of ANNIE. One vertical and one horizontal layer of the MRD (the second and the third layers, respectively) are read. *Layer 2* consists of two sets of 13 horizontal paddles, while *Layer 3* consists of two sets of 15 paddles. The number of needed readout channels from these two subsystems are

- 26 channels for the forward Veto;
- 26 channels for *Layer 2* of the MRD;
- 30 channels for *Layer 3* of the MRD;

for a total of 82 channels.

In place of the full CAMAC electronics implementation (see section ref), the two detectors signals are summed and read by VME electronics (section ref) to give a primary handle on these devices. CAMAC electronics (see section ref) is employed to read these channels.

## Chapter 3

# Data Acquisition system

Modern high energy Physics experiment's require automated procedures to collect data from detectors and save them in long term storage for ensuing analysis. These routines are gathered in automated system called Data Acquisition system (DAQ), which typically includes three fundamental components:

1. sensors, to convert physical parameters to electrical signals;
2. signal conditioning circuitry, to convert sensor signals into a form that can be converted to digital values.
3. conversion from analog signals to digital values and subsequent storage.

The last step is vital in that it allows data manipulation and analysis by a computer.

As far as ANNIE is concerned, the first requirement has already been discussed in section ref: the experiment has multiple simultaneous data sources, i.e. the forward Veto, water PMTs and the MRD, as well as a blend of front-end electronics technologies (VME, CAMAC and custom FADCs) for ADC/TDC and waveform digitisation. Considering this variety of devices, the whole system has also some requirements to achieve:

- stability, on long acquisition runs;
- control all the aspect of the experiment;
- real time online monitoring;
- direct and remote user control.

Provided a solid electronic system, these tasks are thoroughly accomplished on the software's side, since the system is based upon the *ToolDAQ Framework*<sup>1</sup>, developed by Dr Benjamin Richards [ref] for the Hyper Kamiokande collaboration (HK). The HK group has used this opportunity to undertake R&D and testing of DAQ software and tools for future use in the HK experiment. ANNIE experiment has allowed extensive testing of the flexibility of the software and all the above features to take place within a single deployment.

ToolDAQ is designed to incorporate the best features of other frameworks along with:

- being very easy and fast to develop DAQ implementations in a very modular way;
- Dynamic Service Discovery and Publishing;
- scalable network infrastructure (provided by ZeroMQ) to allow its use on large scale experiments.

---

<sup>1</sup>ToolDAQ is open source and available on GitHub [repo].

The main executable relies on user-defined modular classes, called *Tools*, which present three chief functions, *Initialise*, *Execute*, and *Finalise*. The Tools can be daisy-chained to a *ToolChain* and then handled sequentially by the process whenever one of those functions is called. A ToolChain also manages the more complicated aspects of the DAQ system, like the remote control, the service discovery, and the status of the contained Tools. Parameters, data and other variables are passed between Tools by an editable shared data class. Each tool is allowed to read, update, and modify it, due to it is owned by the ToolChain. The bare structure is sketched in Fig. 3.1.

In the following sections, the whole DAQ structure is analysed as it currently is. It is composed of three parallel ToolChains: the Main DAQ Chain, the VME Chain, and the CAMAC/MRD Chain. The latter hasn't been implemented in the Main DAQ system yet, which is composed by the first two Chains only. At the moment the MRD Chain/DAQ is employed as a standalone DAQ, working in parallel with the Main DAQ, on a different machine with resulting difficulties. Future integration of the two DAQ in the same machine are also discussed.

### 3.1 Main DAQ Chain and VME Chain

#### 3.1.1 Hardware

The primary readout for ANNIE Phase I is provided by a VME-based system developed for the KOTO experiment<sup>2</sup> by University of Chicago. The *VMEbus* is a computer architecture, where “VME” stands for VERSA Module Eurocard. It was originally developed by the Motorola, Mostek, and Signetics group, but later was widely used for many applications and eventually standardised by the IEC as ANSI/IEEE 1014-1987. This bus is widely used in High Energy Physics due to the fact that it is of public domain and its data transfer speed is quite fast: for instance the latest manifestation, the VME320/2eSST protocol, can double the theoretical bandwidth of VME to 320MB/s. cite[<http://www.vita.com/VME320-2eSST-Protocol>].

The crates are governed by a VME-based CPU board which runs Internet Rack Monitor software. This latest version runs on the MVME162-22 CPU board with MC68040 CPU, 4MB dynamic ram, 0.5MB static ram, 1MB flash memory, Ethernet interface, and support for up to four Industry-Pack daughter boards. The latter allows connection to I/O signals via ribbon cables to digital and analog interface boards mounted inside the IRM chassis. The Ethernet interface allows network connection and supports widely-used Internet protocols that allow data request and setting access as well as alarm reporting, all based upon the UDP (User Datagram Protocol) transport layer.

The system consists of two types of VME module:

- 4-channel 500 MHz sampling pipeline 14 bit custom FADC cards, which primarily record the traces from the PMTs in the ANNIE water volume.
- Master Trigger (MT) cards which distribute the 125 MHz clock, synchronises the FADC cards, provides the trigger, and provides a busy signal.

<sup>2</sup>The KOTO experiment at J-PARC, Japan, aims at observing the rare kaon decay  $K_L \rightarrow \pi^0 \bar{\nu} \nu$  to search for new physics beyond the standard model that breaks the CP symmetry. The experiment, with a new beam line and new detector components, is underway and the first run was performed in May 2013.

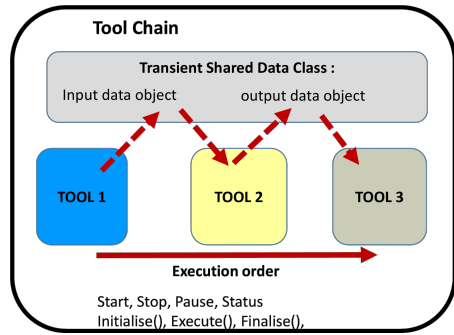


Figure 3.1: Schematic of a ToolChain.

The leading edge of photomultiplier signal is too fast for an 8-ns sampling. To avoid dead time and allow the 500 MHz sampling, the output signals from the detectors are stored in 8000 samples pipelines inside Field Programmable Gate Arrays (FPGAs) until a trigger decision is made. The three levels trigger system uses the waveform information with increased sophistication at each level. Each MT card can address 8 FADC cards, but can be daisy-chained or arrange hierarchically to address more total cards. Given the 16 FADC cards of the ANNIE readout, 3 MT cards are used: one Level-0 card distributes the clock between two Level-1 MT cards, each addressing 8 FADCs.

The Muon Range Detector and the Forward Veto nominally rely on the same FADC system as the PMTs in the water volume for the first runs. The signals coming from the paddles are combined through an analog OR and sent to a few spare FADC channels on the KOTO boards.

The instrumenting the ANNIE water volume are operated at positive HV with a single cable for both power and signal. Splitter boxes will be necessary to separate the PMT signal and the HV. ANNIE uses a CAEN system to provide the positive and negative high voltages necessary for operation. A stock of 6 A734P cards suffices to power the 62 large PMTs in the water volume and the 26 positive HV PMTs in the MRD. 26 negative HV channels are also needed for the Forward Veto and another 52 channels to power at least two layers of the MRD.

For storage limitations, a down-sampling to 125 MHz was established. The resolution of 8 ns suffices the needs of the R&D stage of Phase I. An 80  $\mu$ s long time window wash chosen, therefore with this resolution, four data sets can be hold in the 40000 samples buffer. Each set corresponds to a spill from the beam.

### 3.1.2 Software

The data from the water PMTs and the logical sum from the Veto and MRD are acquired by the Main DAQ, which hinges upon two strictly complementary ToolChains: the Main Chain and the VME Chain. The Main Chain is the primary ToolChain of the DAQ system, which communicates with the other two processes.

The Chain's tools are depicted in Fig. 3.2 and they are the following:

| Main DAQ             | VME               |
|----------------------|-------------------|
| Input variables      |                   |
| PostSQL              | VME Trigger Send  |
| Trigger              | Board Reader      |
| Network Receive Data | Network Send Data |
| Monitor              |                   |
| Data Recorder        |                   |

The *Input variables* tool loads some initialisation parameters and the specification of the current *run*, i.e. data taking session. Three typologies of run are available and are sent to the VME CPU: a test run, an LED run for PMTs calibration, a pedestal run, and a beam run. The triggering of the digitisers is influenced by changing the kind of the run. For instance, a beam run is triggered by the RWM, while an LED run is triggered by the LED pulser. The *PostSQL* tool updates an SQL database of the DAQ, where all the information about the run, such as the number of events, the start and the stop time, and others, are saved. Proper data logging is a fundamental step, especially for Phase I: both the experiment and the DAQ are frequently revised and **knowing which run is which is pretty cool**. *Trigger* tool blocks the Chain, awaiting and sending a trigger query from the VME. When the VME replies, the Chain is run back again. As explained, four 10000samples data sets are collected from the VME cards, which equates to four

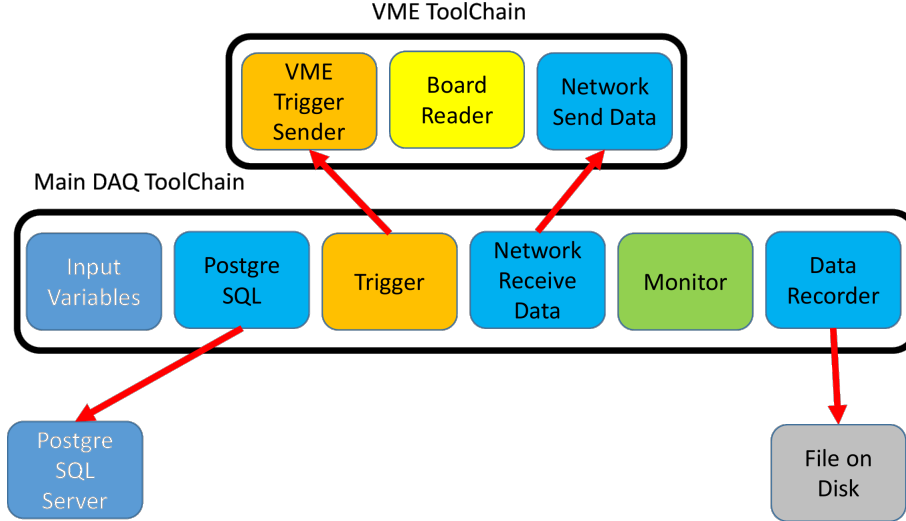


**Figure 3.2:** ANNIE’s current main DAQ makes use of two parallel tool chains.

consecutive spills from the beam. The *Network receive data* tool handles the data transfer via ZeroMQ messaging<sup>3</sup> between the main chain and the VME one. Like most of the HEP experiments, even ANNIE requires real-time monitoring so as to check whether the DAQ system works flawlessly. This is achieved by the *Monitor* tool, which updates a dedicated web-page with random plots of data collected.

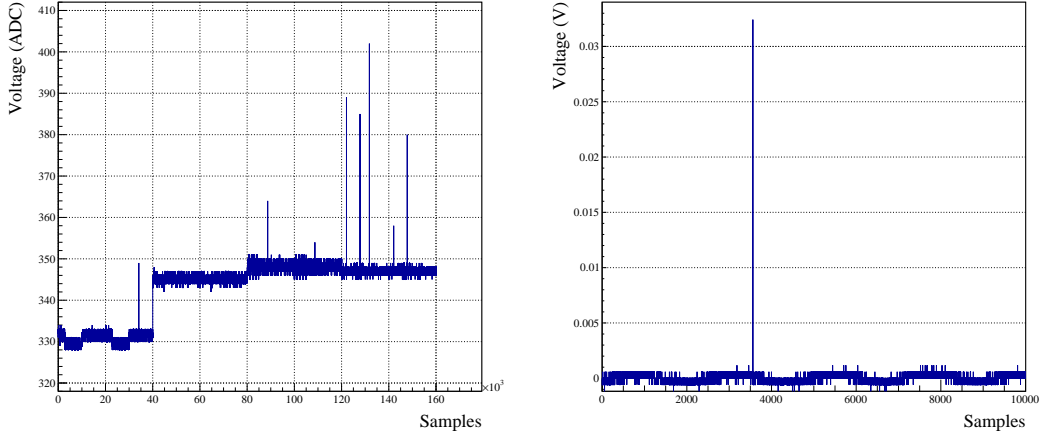
On the VME electronics side, the Chain communicates with the VME CPU retrieving all the information about the cards and the trigger. The *Trigger Sender* tool check the status of the VME controller. If the ADC are triggered, a trigger message is sent to the Main Chain. The data are dumped from the FPGA’s buffer by the *Board Reader* tool and are sent to the Main Chain via ZeroMQ messaging over TCP.

The last tool of the Main Chain, *Data recorder*, saves data into the following ROOT tree structure:

**LastSync** : time of data acquisition;  
**SequenceID** : incrementale number;  
**StartTime** : same as lastsync;  
**CardID** : number of ADC card;  
**Channels** : channel of ADC card;  
**PMTID** : global identifier of PMT (labelled from 1 to 60);  
**BufferSize** : size of the buffer per channel;  
**FullBufferSize** : size of the buffer per card;  
**Data** : an array holding the full buffer of a single card.

Each entry corresponds to an acquisition of the full buffer from the cards saved in a 160000 long float array, i.e. the digitised time profile of four consecutive 80  $\mu$ s data set times the four channels. The ROOT files are then post processed: the buffer is split

<sup>3</sup>*ZeroMQ* is a high-performance asynchronous messaging library, aimed at use in distributed applications. The API provides *sockets*, each of which can represent a many-to-many connection between endpoints, operating with a message-wise granularity. ZeroMQ is developed by a large community of contributors and distributed under the LGPL license. <http://zeromq.org/>



(a) Before post-processing, arrays include the full buffer from each card.

(b) After post-processing, arrays are split per trigger and hold 80  $\mu$ s worth of data.

**Figure 3.3:** Time profile before and after the post-processing.

and an entry is created for each beam event, or trigger, and the precise time stamp is reconstructed. In Fig. 3.3 the time profile is shown before and after the post-processing. Moreover, each channel is mapped to its equivalent PMT. This stage reduces the file sizes by a nearly a factor of four.

Provided that the spill’s frequency is  $\sim$ 15 Hz and four spills are acquired, the buffer takes around a quarter of a second to fill. The longest portion of the chain to execute is the disk saving and it is meant to be done between pulse trains, so as to minimise the number of spills lost. A whole execution of the chain lasts nearly a second, slightly less than the pulse train frequency.

## 3.2 MRD Chain

### 3.2.1 Hardware

As explained in Sec. 3.2[edit to section of VME], the signal from the FACC and two layers of the MRD are logically summed and read by the VME digitisers. The PMTs of these two detectors are supposed to be read individually by both Time-to-Digital Converters (TDC) and ADCs in future stages of the experiment and for this purpose a third ToolChain has been developed to collect data from both the VETO and the MRD’s second and third layers (see section ref). CAMAC electronic modules are employed for these two detectors: LeCroy 3377 modules for the time digitisation, while LeCroy 4300B for analog conversion.

*Computer-Aided Measurement And Control* (CAMAC) is a bus and modular-crate electronic standard for data acquisition and control used mainly in nuclear and particle physics experiments and in industry. The bus allows data exchange between plug-in modules and a crate controller, which then interfaces to a CPU or to a VME-CAMAC interface. The standard was originally defined by the ESONE Committee as standard EUR-4100 in 1972.

The LeCroy Model 3377 is a 32-channel time-to-digital converter (TDC) and optimised with a low conversion time and a high speed readout of 100 ns/word. With 10-bit words, the longest time window achievable is 4088.0 ns, using a resolution of 4.0 ns. A delayed signal from the RWM acts as a “common start” for the TDC cards and each internal counter is individually stopped by hit signals. The channels are fed with the discriminated PMT

signals of the VETO and of the second and the third layer of the MRD.

The LeCroy Model 4300B FERA contains 16 independent 11bit charge-to-digital converters. An 8-bit register and a memory containing the individual pedestal values to be subtracted from each ADC are also available. These converters haven't been installed in the electronic chain yet. Nevertheless the software interface has been developed anyway.

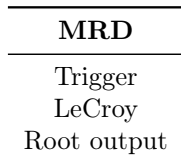
All the cards are addressed via the Weiner CCUSB controller module. The CCUSB is a full-featured CAMAC Crate controller with integrated high speed USB-2 interface. For fast data acquisition applications the CCUSB has a built-in command list sequencer, called *command stack* with data buffering in a 22kB size FIFO. A XILINX Spartan 3 family FPGA performs all CCUSB logic and functions. [More on this?](#)

### 3.2.2 Software

The thesis's work is mainly focused on the development of a dedicated data acquisition system for the CAMAC electronics of the experiment. A separate MRD DAQ has been created from scratch within the ToolDAQ Framework in order to acquire the MRD and the forward Veto data. These two detectors rely on the CAMAC electronics for front-end read out of the PMTs signals and the USB controller vendor provides a C++ class to interface the controller with the computer.

Some C++ classes were developed with the purpose of handling more easily the modules. A base class takes care of opening the USB connection for the CCUSB controller and storing information on the cards, such as the Slot number. It also allows the configuration of the command stack, i.e. the CAMAC command sequencer. Two derived classes implement wrapper functions to deliver CAMAC commands via the NAF addressing<sup>4</sup>.

The MRD's ToolChain employs the CAMAC classes to interface with the controller and the cards. As illustrated in Fig. 3.2, the Tools contained in the Chain are: [picture of MRD chain alone](#).



The *Trigger* tool reads the FIFO of a specified card: if it is not empty, then all cards presenting data are read and other tools are executed. Currently, a hit signal is generated in each TDCs by delaying the common start signal of  $\sim 1 \mu\text{s}$ , such that the FIFOs are never empty in coincidence with the beam's spills. Three triggering behaviours are supported: external trigger, software trigger with random card access, and software trigger with card test function.

The *LeCroy* tool is meant to work for both the TDCs and ADCs cards. If only either TDCs or ADCs are employed, then only one tool should be added in the *ToolChain*. Otherwise, if both are used, then two *LeCroy* tools are required. Given that the ADCs haven't been installed in the crates yet, only one tool is needed for the TDCs. Nevertheless the charge converters have been tested, as well.

The last tool fills a ROOT tree and save it to file. The tree has the following branches:

**Trigger** : incremental number of the trigger;

**OutNumber** : number of channels read;

**Type** : string telling whether the data refer to TDC or to ADC;

---

<sup>4</sup>Module addressing is achieved knowing the slot Number, the subAddress, and the Function code.

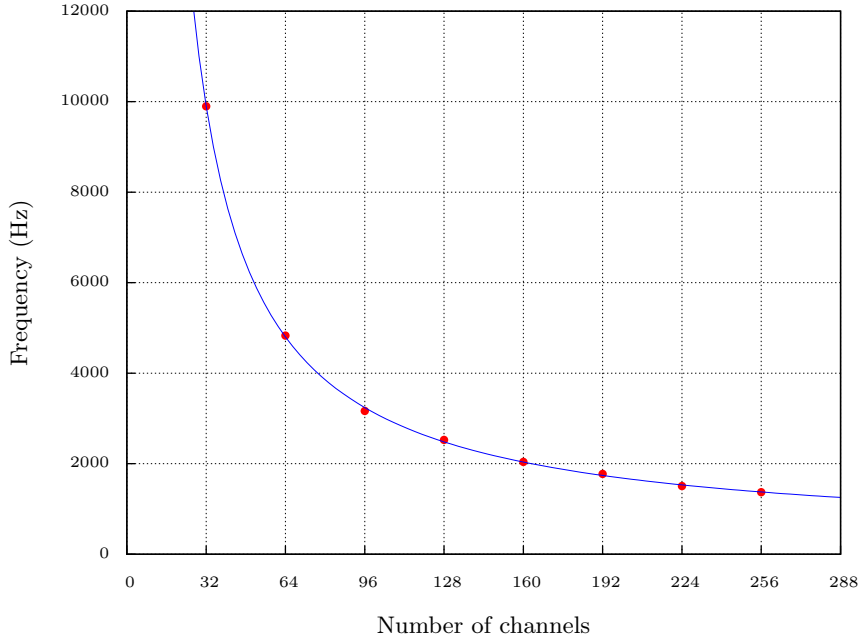


**Figure 3.4:** DAQ frequency reading TDCs with all channels fired, but 1.6% time occupancy.

**Value :** actual value retrieved from the card.

**Slot :** slot number of the card;

**Channel :** channel of the card from which the value was retrieved;

**TimeStamp :** UNIX time stamp of the entry, since epoch, in ms.

The MRD Chain runs in a different PC than the Main DAQ and the ToolChain is executed at a different speed, for it is a standalone process. For this reason, a method has been realised to correlate the events between the two DAQs. Timestamps were designated for this fundamental task: both DAQs assign UNIX time to each event, since the clocks are synchronised to the same NTP server, which uses GPS time sources. With the help of the Fermilab spill database [ref here], the events from the two DAQs can be related to each other.

This method is effective as long as the frequency of the chain execution is greater than the spill frequency. The frequency should be above the 15 Hz spill frequency in order not to miss any beam event. However the CAMAC event rate has been found to be quite low in this early stage, around 0.20 Hz<sup>5</sup>, since only two layers of the MRD are used, in addition to the Veto. This suggest that the modules present data only the ~1.3% of the time.

Concerning the MRD DAQ, the longest portion of the chain is the CAMAC addressing and data collecting. The software has been tested using software triggering, employing the test functions of the modules, and counting the time required for 100,000 repeated cycles with 1.3% firing probability; the frequency was afterwards estimated. The result is shown in Fig. 3.4, where frequency vs number of channel is plotted for TDC modules. It's clear that the frequency is well above the lower theoretical limit of 15 Hz. Rescaling the frequency to full time firing, i.e. the number of channel to be read is maximum for every DAQ cycle, the limit is easily reached with just ten modules, corresponding to five layers of MRD, Veto excluded.

<sup>5</sup>The rate is measured from output ROOT file, dividing the number of entries, i.e. events, by the time passed between the first and the last TimeStamp.

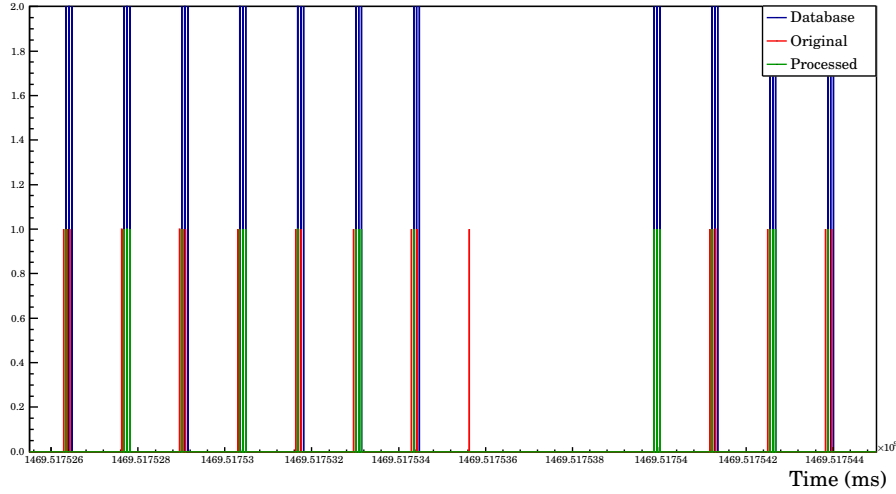


**Figure 3.5:** Detail of the time stamp alignment with the database data.

For these reasons, the command stack of the CCUSB controller is not employed, because the USB connection can provide fast enough communication to address all the active cards.

Concerning the TimeStamp, a time variable drift in the MRD TimeStamps has been found, likely due to imprecise synchronisation with the NTP server (accuracy given to be less than 30 ms) which occurs every 1024 ms. A post-processor has been written to fix the TimeStamps, identifying time patterns in the spill spectrum and comparing them to the database information. In Fig. 3.5 a detail of the result of the synchronisation is plotted. The blue lines are given by the database, used as a reference. The TimeStamps before and after the post-processing are printed respectively in red and green.

The post-processor also handles other aspects of the raw data, like converting the module's values into physical quantities and mapping each channel to its PMT.

### 3.3 Future improvement

Down-sampling -> was it worth it? Zero suppression is cooler for memory issues, takes a lot of memory.

Integration between Chains, using TimeStamps now and database. This technique is ok, but the chains must be implemented better each other.

One solution could be to create a tool to govern the MRD chain, as in Fig. 3.6

The final version of the DAQ system needs a full integration of the Main Chain with the CAMAC one. A possible solution is depicted in Fig. 3.6. A new tool could be employed to embody a simplified version of the MRD ToolChain, rather than run it in a parallel process. The MRD Chain, as proved in previous sections, is fast in execution, so it should not significantly slow down the Main DAQ. In this way, the TimeStamp synchronisation technique is not required anymore because all the acquisitions are done by the same CPU and simultaneously. As far as the output files are concerned, the ROOT trees could be merged into a single ROOT file triggering the two recording tools with ZeroMQ communication. Final reconstruction of PMTs data and MRDs could be done in a post-processing stage.

In view of the next phases of the experiment, an other DAQ-related issue is the memory storage. During early test runs, the digitiser would sample at a frequency of 500 MHz, but it has been promptly downgraded to 125 MHz because of lack of long term memory storage. As a matter of fact, noise is mostly shown in the 80  $\mu$ s time window and the meaningful

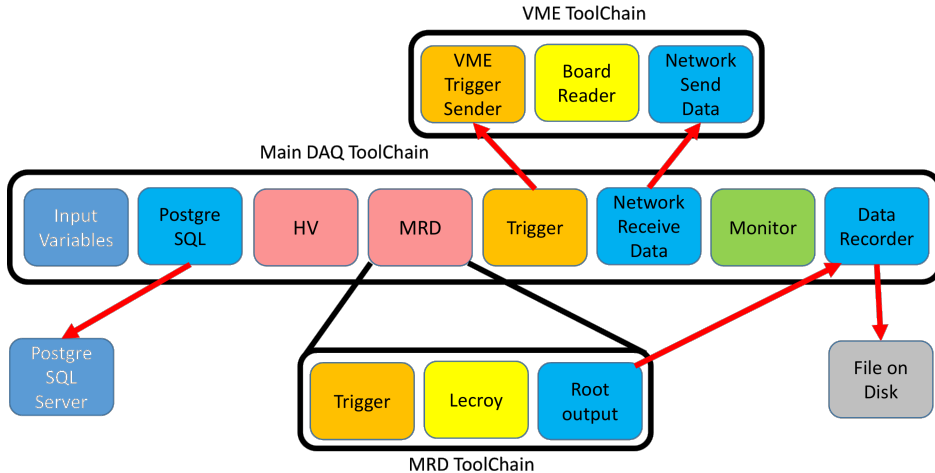


**Figure 3.6:** Final version of ANNIE's DAQ, with all the Chains integrated.

signal is limited short, compared to the time window. Considering that an high time resolution is pointless in the R&D stage of the experiment, the downgrade was established. Soon, *zero-suppression* method would be employed, which will definitely overcome storage needs. The preliminary data analysis undertaken can back this decision up, as explained in section [ref].



## Chapter 4

# Data Analysis procedures

Early stage data have also been analysed. In particular, event reconstruction techniques were developed and tested from scratch: they are implemented in a purpose-built data analysis software, which studies signals acquired from the water PMTs. The code's algorithm relies on individual pulse analysis and it is largely focuses on the rejection of background with respect to event signals. These data analysis procedures are illustrated in this chapter, while meaningful results are presented in the following chapter. Some of the methods could be employed into a more complete analysis framework, valid even for the future phases of the experiment.

The Main DAQ (see section ref) is programmed to create a new *Run* every time the Chain is stopped and restarted. Due to being an R&D phase, the DAQ has been improved in various occasion during data taking, hence the size and the number of post-processed files, that constitute the *Runs*, are not constant. Each file is a ROOT file containing the PMT data collected, in the way explained in section ref. The buffer retrieved from the VME boards is properly split for each trigger signal, in that each set of data consists of  $80 \mu\text{s}$  worth of digitised signal. A file holds 383 full buffers and this translates to 1532 triggers: the effective time carried by a single file is 122.560 ms.

### 4.1 Individual pulse analysis

The data analysis software scans all the post-processed time profile which the *Run* consists of, as the one shown in Fig. 4.1, sorted by trigger and PMT number. Any peak above a certain voltage threshold,  $V_T$ , is selected and an enclosing time window of a predefined length,  $L$ , is trimmed around it. A length of  $L = 100$  samples was chosen, resulting in a  $0.8 \mu\text{s}$  long window. The position of the peak inside this window was set to 20% of its length, i.e. the peak is always set at  $0.16 \mu\text{s}$  from the beginning of the time window. These subsets of data are being called *pulses* and are collected in another ROOT file. The choice of window length and the peak position is the result of a compromise between speed of the code, memory usage and loss of physical information. In fact, many pulses shows consecutive multiple peaks, as the one in Fig. 4.2, mainly given by light reflections in the water tank.

Each pulse is individually analysed and processed by a routine of algorithms. As a result, a set of values, typical of the pulse<sup>1</sup>, are gathered from every pulse, in addition to Veto and MRD coincidences. These quantities, outlined in Fig. 4.3, are useful for following analysis and they are:

**Baseline** is given by the average of first 10 points of the pulse; this value is then subtracted from the whole array.

---

<sup>1</sup>I don't like this.

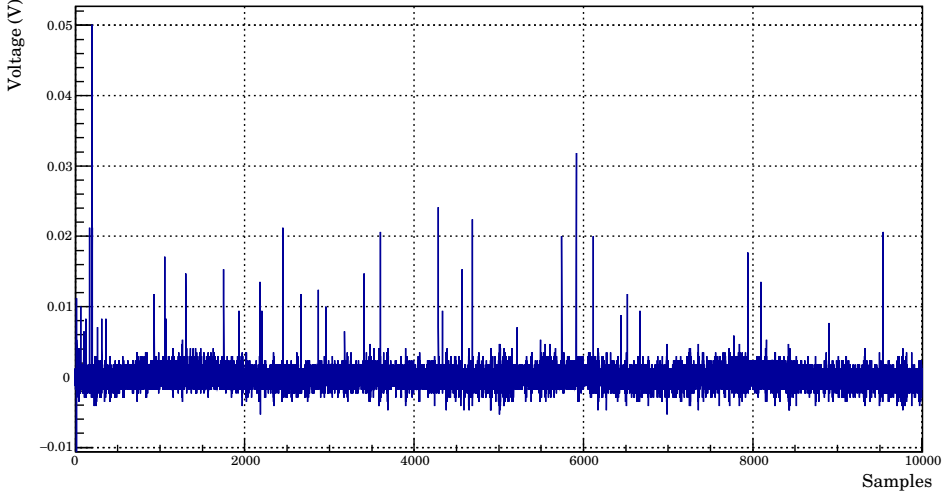


**Figure 4.1:** Time profile of a single trigger: the signals of the sixty PMTs are here overlaid.

**Height** is the height of the peak (maximum) with respect to the zero.

**Peak to valley** it is the time distance from the peak to the valley (minimum);

**Start** is position of the 25% of the rising edge of the pulse, estimated with precision using cubic interpolation.

**Width** is the time that spans from Time to the 5% of the falling edge of the pulse, calculated using the same algorithm employed for Time.

**Charge** is the sum of the 5 points around peak, weighted by the bin width.

**Energy** is the sum of the points from Time to Time+Width, with bin weight.

**Area** is the area of the modulus of the pulse.

**Time of flight** is the time difference between Time and RWM signal.

**Previous** is the Time of the previous pulse, if from the same PMT.

## 4.2 Event definition

For every Trigger, the time distribution of the peaks is also studied, as well as the time coincidences between the PMTs signals: a time allowance of  $0.8 \mu\text{s}$  is considered to count of pulses happening simultaneously; this easily translates to the number of PMTs fired at the same time. When the latter exceeds a defined threshold,  $N_{PMT}$ , then an *Event* is appointed and its precise time position is afterwards estimated by a weighted average of the adjacent coincidences. The multiplicity of an Event is a good indicator of the nature of the detected interaction. As discussed in section ref{sec:background}, a cosmic muon, likely coming from above, would project the Cherenkov radiation on the bottom of the tank, thus lighting the majority of the water PMTs. On the other hand, a muon arisen from the interaction of a beam neutrino with a nucleon would emit gammas along the beam direction: only a

<sup>1</sup>The algorithm looks for four points around the threshold which are used to define a cubic function. Using Newton's method, the time position is found.

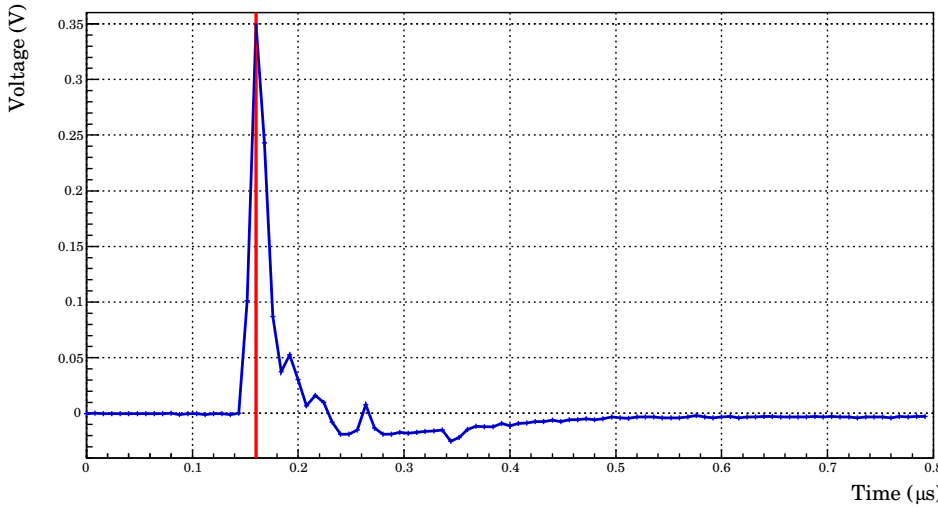
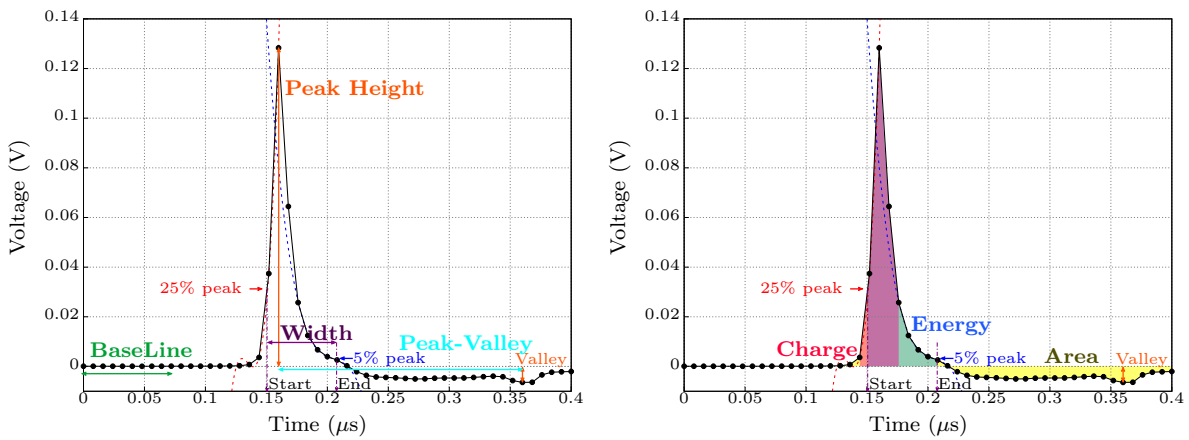


**Figure 4.2:** Time profile of a single pulse. The red line marks the 20 % of the window's length, at  $0.16 \mu\text{s}$ . The first peak and the second peak are about forty nanoseconds apart, which is the time needed for the light to travel back and forth inside the tank (see section ref).



**(a)** From left to right: in green the *BaseLine*, in orange the *Peak Height*, in purple the *Width*, and in light blue the *Peak to Valley* time distance.

**(b)** From left to right: in pink the *Charge*, in blue the *Energy*, and in gold the *Area*. These three integrals cross over each other in the purple region.

**Figure 4.3:** Illustration of the pulse analysis values. The 25 % and 5 % *peak height* marks, which define the *Start* and *End* of the signal, are common to both diagrams. The dashed lines represent the cubic interpolations.

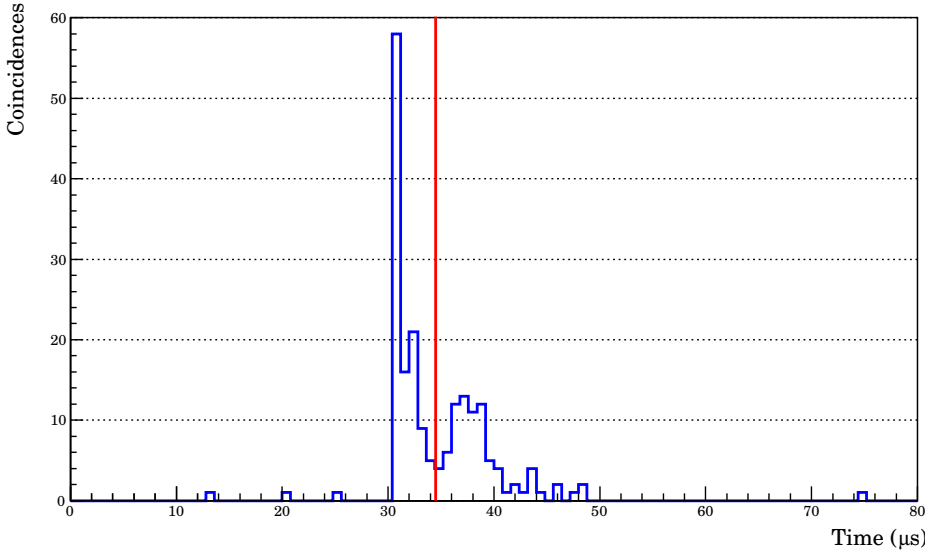


**Figure 4.4:** This histogram is filled with the Start time of each pulse belonging to the same trigger. A high multiplicity is found near  $31\ \mu\text{s}$ . In this particular case, the time distribution of the signals is quite long: the light in the tank lasts for about twenty microseconds. The red line marks the weighted average of the coincidences, which is  $34.51\ \mu\text{s}$  in this example.

portion of the light cone could be captured. Even natural radioactivity, from radionuclide in the glass of the phototubes, can trigger some detectors, although this event are readily filtered by a proper value of  $N_{PMT}$ . An high-multiplicity event is exemplified in Fig. 4.4.

### 4.3 Signal and noise discrimination

**Bad english here.** Not all the pulses found in a trigger belong to the Event. For instance, in Fig. 4.4 there are four pulses far from the main pulse cluster. These might be likely generated by noise sources and therefore they are meaningless. In order to discriminate the pulses, time window is defined around the Event time position. Every pulse that falls within this interval is designated as a *signal*; otherwise it is *noise*.

I need a picture of the rejection time window and a picture of  $N_{PMT}$  freq.

Discriminating signal from background is a step of utmost importance for data analysis. In order to find the best value of the parameter (see section ref), these have been varied, thus the data have been analysed various times. Twelve combination were chosen and they are listed in Tab. 4.1.

### 4.4 Data selection

Being an R&D stage, the data acquisition has not been methodic and continuous, but notwithstanding high statistics were achieved most of the time. Three distinctive couples of consecutive runs were selected as model data set, with the intention to outline the best data analysis procedures. These are

**Table 4.1:** The combination of the employed thresholds are here listed.

| $V_T$<br>(V) | $N_{PMT}$ | $\Delta_T$<br>( $\mu\text{s}$ ) |
|--------------|-----------|---------------------------------|
| <b>0.02</b>  | <b>10</b> | <b>4.0</b>                      |
| 0.005        | 10        | 4.0                             |
| 0.01         | 10        | 4.0                             |
| 0.05         | 10        | 4.0                             |
| 0.10         | 10        | 4.0                             |

**Table 4.2:** Runs selected for data analysis. They are composed of different numbers of file, resulting in diverse number of triggers. Total time is the number of triggers times 80  $\mu\text{s}$ . The listed memory sizes refer to the post-processed files.

| Run | N of files | N of Triggers | Total time<br>(ms) | Data size<br>(MB) |
|-----|------------|---------------|--------------------|-------------------|
| 93  | 88         | 134,816       | 10,785.280         | 65,027.961        |
| 94  | 54         | 82,728        | 6618.240           | 41,102.486        |
| 120 | 43         | 65,876        | 5270.080           | 19,887.893        |
| 121 | 15         | 22,980        | 1838.400           | 6735.270          |
| 145 | 80         | 122,560       | 9804.800           | 37,204.525        |
| 146 | 84         | 128,688       | 10,295.040         | 39,050.909        |

**R93/R94** beam off, trigger random

**R120/R121** after card synchronisation

**R145/R146** PMT mounted on NCV

and their characteristics are shown in Tab. 4.2.



# Chapter 5

## Data analysis results

I feel like basing all this chapter upon the parameters variation.

Some results regarding the validity of the selection method, discussed in the previous chapter, are presented here.

Using the techniques described in the previous section, the selected data sets are studied (see section ref) in order to test the validity of the selection method proposed. The rate of cosmic is also evaluated, as well as the muon lifetime and the neutron yield

### 5.1 Cosmic background data

The idea here is to compare expected muon rate with measured one.

High energy particles, mainly originated outside the Solar System and thus called *Cosmic Rays*, impact on the Earth's atmosphere and producing mesons, which in turn generate secondary particle shower by decaying. The primary particles are about 99% made of ionised nuclei (79 % protons, 19 % alphas, 2 % heavier nuclei), while the remaining 1 % is mostly composed by electrons. The intensity of the nucleons in the energy range from several GeV to somewhat beyond 100 TeV is given approximately by

$$I_N(E) \simeq 1.8 \times 10^4 \left( \frac{E}{1 \text{ GeV}} \right)^{-\alpha} \frac{\text{nucleons}}{\text{m}^2 \text{ s sr GeV}}, \quad (5.1)$$

where  $E$  is the energy-per-nucleon, including rest mass energy, and  $\alpha = \gamma + 1 = 2.7$  is the differential spectral index of the cosmic ray flux, with  $\gamma$  the integral spectral index.

Many are the secondary products reaching the sea level, among which muons, neutrinos, nucleons, and electrons. The first two, muons and neutrinos, derive from the decay chain of charged mesons, while electrons and photons originate in decays of neutral mesons.

As Fig. 5.1 shows, muons are the most numerous charged particles at sea level. Muons lose energy to ionisation at a fairly constant rate of about 2 MeV per g/cm<sup>2</sup>. Given that the vertical depth of the atmosphere is about 1000 g/cm<sup>2</sup>, muons will lose about two GeV before reaching the ground. The mean energy of muons at sea level is about four GeV; therefore the mean energy at creation, typically fifteen kilometres high, is probably near six GeV. Their energy and angular distribution reflect a convolution of the production spectrum, energy loss in the atmosphere, and decay. The energy spectrum is almost flat below 1 GeV, steepens gradually to reflect the primary spectrum in the 10÷100 GeV range, and steepens further at higher energies because pions with  $E_\pi > \epsilon_\pi$  tend to interact in the atmosphere before they decay, where  $\epsilon_\pi = 115$  GeV is the critical decay energy for pions. Asymptotically ( $E_\mu \gg 1$  TeV), the energy spectrum of atmospheric muons is one power steeper than the primary spectrum. The integral intensity of vertical muons above 1 GeV/c at sea level is nearly  $70 \text{ m}^{-2} \text{s}^{-1} \text{sr}^{-1}$  [41,42], with recent measurements [43–45] favouring a lower normalisation by 10-15 %. Another way to express this evaluation is the

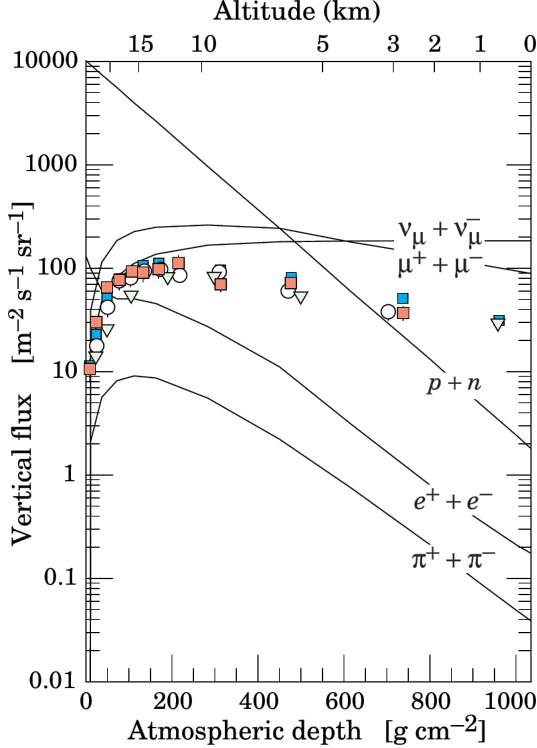


**Figure 5.1:** Vertical fluxes of cosmic rays in the atmosphere with  $E > 1$  GeV estimated from the nucleon flux of Eq. 5.1. The points show measurements of negative muons with 1 GeV from ref[32–36].

form

$$I_0 \simeq 1 \text{ cm}^{-2} \text{ min}^{-1} = 166.7 \text{ m}^{-2} \text{ Hz}, \quad (5.2)$$

for horizontal detectors. The overall angular distribution of muons at the ground is  $\propto \cos 2\vartheta$ , which is characteristic of muons with  $E_\mu \sim 3$  GeV.

With the beam off, only cosmic rays and background leave a trace in the detector. Therefore runs 93 and 94 are useful to characterise the background.

From Eq. 1.2, every muon with an energy  $E > 159.739$  MeV can produce Cherenkov radiation, given that the refractive index of water is  $n = 1.33$  and the muon mass is 105.658 MeV<sup>1</sup>. Since the average energy of the muon reaching the ground is well above the Cherenkov threshold, the nominal flux at sea level can be used to evaluate the cosmic background rate. The water tank is placed eight meters below the surface, and it fits the hall's walls, hence only the top area of the tank (slightly more than 7 m<sup>2</sup>) could be taken in consideration. A rough estimation suggests that the number of muons reaching the detector is

$$I \simeq 7 \text{ m}^2 I_0 \simeq 1178.1 \text{ Hz}. \quad (5.3)$$

From the runs selected...

## 5.2 Threshold dependence

Three parameters of the Data Analysis software have been tuned so as to study the feedback of the rejection method. The parameters are:

1. Voltage threshold;
2. Number of PMTs fired;

<sup>1</sup>The muon mass is known with an accuracy of order  $10^{-8}$ . According to the PDF,  $m_\mu = 105.658,371,5 \pm 0.000,003,5$  MeV.

3. Time rejection window.

Loads of tables here: something about final size and zero-suppression,...

#### **5.2.1 Voltage**

#### **5.2.2 PMTs fired**

#### **5.2.3 Rejection window**

### **5.3 Michel decay**

I've seen it, it could be a nice plot to place here.

### **5.4 Neutron yield**

No luck yet. really not sure whether or not include this section.

### **5.5 First MRD data**

TDC, could do some dummy analysis.



# Chapter 6

## Conclusions



## Appendix A

# Booster Neutrino Beam

Arxiv 1311.5958v1. Fermilab has two major neutrino beamlines: the Neutrino Main Injector (NuMI) and the Booster Neutrino Beam (BNB). The energy range of these two neutrino sources on-axis is in the GeV range, which is too high to satisfy the condition for dominance of coherent scattering. The far-off-axis ( $> 45^\circ$ ) of the BNB produces well defined neutrinos with energies below 50 MeV. The BNB source has substantial advantages over the NuMI beam source owing to suppressed kaon production from the relatively low energy 8 GeV proton beam on the target ref. Therefore, pion decay and subsequent muon decay processes are the dominant sources of neutrinos. At the far-off-axis area, the detector can be placed close enough to the target to gain a large increase in neutrino flux due to the larger solid angle acceptance.

### A.1 BNB details

An initial study using the existing BNB MC has confirmed that this approach is promising. The Fermilab Booster is a 474-meter-circumference synchrotron operating at 15 Hz. Protons from the Fermilab LINAC are injected at 400 MeV and accelerated to 8 GeV kinetic energy. The structure of the beam is a series of 81 proton bunches each with a 2 ns width and 19 ns apart. The maximum average repetition rate for proton delivery to the BNB is 5 Hz and  $5 \times 10^{12}$  protons per pulse. The repetition limit is set by the horn design and its power supply. The target is made of beryllium divided in seven cylindrical sections in a total of 71.1 cm in length and 0.51 cm in radius. In order to minimize up-stream proton interactions, the vacuum of the beam pipe extends to about 152 cm upstream of the target. The horn is an aluminum alloy toroidal electromagnet with operating values of 174 kA and maximum field value of 1.5 Tesla. A concrete collimator is located downstream of the target and guides the beam into the decay region. The air-filled cylindrical decay region extends for 45 meters. The beam stop is made of steel and concrete.

PHYSICAL REVIEW D 79, 072002 (2009). The Fermi National Accelerator Laboratory (FNAL) booster is a 474-meter-circumference synchrotron operating at 15 Hz. Protons from the Fermilab LINAC are injected at 400 MeV and accelerated to 8 GeV kinetic energy (8:89 GeV=c momentum). The booster has a harmonic number of 84, of which 81 buckets are filled. The beam is extracted into the BNB using a fast-rising kicker that extracts all of the particles in a single turn. The resulting structure is a series of 81 bunches of protons each 2 ns wide and 19 ns apart. Upon leaving the booster, the proton beam is transported through a lattice of focusing and defocusing quadrupole (FODO) and dipole magnets. A switch magnet steers the beam to the main injector or to the BNB. The BNB is also a FODO that terminates with a triplet that focuses the beam on the target. The design and measured optics of BNB are in agreement [7,8]. The maximum allowable average repetition rate for delivery of protons to the BNB is 5 Hz (with a maximum of 11 pulses in a row at

15 Hz) and  $5 \times 10^{12}$  protons-per-pulse. The 5 Hz limit is set by the design of the horn (described below) and its power supply.

The target consists of seven identical cylindrical slugs of beryllium arranged to produce a cylinder 71.1 cm long and 0.51 cm in radius. The target is contained within a beryllium sleeve 0.9 cm thick with an inner radius of 1.37 cm. Each target slug is supported within the sleeve by three “fins” (also beryllium) which extend radially out from the target to the sleeve. The volume of air within the sleeve is circulated to provide cooling for the target when the beam line is in operation. The target and associated assembly are shown in Fig. 2, where the top figure shows an exploded view of the various components (with the downstream end of the target on the right), and the bottom shows the components in assembled form. The choice of beryllium as the target material was motivated by residual radioactivity issues in the event that the target assembly needed to be replaced, as well as energy loss considerations that allow the air-cooling system to be sufficient. Upstream of the target, the primary proton beam is monitored using four systems: two toroids measuring its intensity (protons-per-pulse), beam position monitors (BPM) and a multiwire chamber determining the beam width and position, and a resistive wall monitor (RWM) measuring both the time and intensity of the beam spills. The vacuum of the beam pipe extends to about 5 feet upstream of the target, minimizing upstream proton interactions. The toroids are continuously calibrated at 5 Hz with their absolute calibrations verified twice a year. The calibrations have shown minimal deviation ( $< 0.5\%$ ). The proton flux measured in the two toroids agree to within 2%, compatible with the expected systematic uncertainties. The BPMs are split-plate devices that measure the difference of charge induced on two plates. By measuring the change in beam position at several locations without intervening optics, the BPMs are found to be accurate to 0.1 mm (standard deviation). The multiwire is a wire chamber with 48 horizontal and 48 vertical wires and 0.5 mm pitch. The profile of the beam is measured using the secondary emission induced by the beam on the wires. The RWM is located upstream of the target to monitor the time and intensity of the proton pulses prior to striking the target. While the data from the RWM did not directly enter analysis, it allowed many useful cross checks, such as those shown in Fig. 3. The left figure shows a comparison of the production times of neutrinos observed in the MiniBooNE detector estimated based on the vertex and time reconstructed by the detector and subtracting the time-of-flight. This time is then compared to the nearest bucket as measured by the RWM. The distribution indicates that neutrino events can be matched not only to pulses from the booster, but to a specific bucket within the pulse. The tails of the distribution result from the resolution of the vertex reconstruction of the neutrino event in the detector, which is needed to determine the time of the event and correct for the time-of-flight. The right plot demonstrates the synchronization of the horn pulse (described in Sec. II C) with the delivery of the beam as measured by the RWM.

The horn current pulse is approximately a half-sinusoid of amplitude 174 kA, 143 s long, synchronized to each beam spill.

The typical beam alignment and divergence measured by the beam position monitors located near the target are within 1 mm and 1 mrad of the nominal target center and axis direction, respectively; the typical beam focusing on target measured by beam profile monitors is of the order of 1–2 mm [root mean square(RMS)] in both the horizontal and vertical directions. These parameters are well within the experiment requirements. The number of protons delivered to the BNB target is measured for each proton batch using two toroids located near the target along the beam line. The toroid calibration, performed on a pulse-by-pulse basis, provides a measurement of the number of protons to BNB with a 2% accuracy. Primary protons from the 8 GeV beam line strike a thick beryllium target located in the BNB target hall.

The SciBooNE hall is on axis from the Booster Neutrino Beam (BNB) at 8 m below the

surface. The BNB impinges 8.89 GeV/c protons from the booster on a beryllium target, with 4 x10to12 delivered in a narrow spill of approximately 1.6 micros at a frequency of 7.5 Hz. The projected number of protons incident on the target (POT) per year for the BNB is about 2 x 10to 20 POT. The rates expected per year when running in neutrino mode for 1 ton of water (the approximate usable fiducial volume) are about 16K neutrino interactions, where 11K of those would be numu CC interactions. This spectrum peaks ideally in the region of interest at 700 MeV as shown left of Figure 2 and has the target rate of neutrino interactions per year. The spectrum and rates are based on BNB flux simulated data provided by Zarko Pavlovic (FNAL)appropriately propagated to the SciBoone hall.

The target is made of seven cylindrical slugs for a total target length of 71.1 cm, or about 1.7 inelastic interaction lengths. The beryllium target is surrounded by a magnetic focusing horn, bending and sign-selecting the secondary particles that emerge from the interactions in the target along the direction pointing to the SciBoone detector. The focusing is produced by the toroidal magnetic field present in the air volume between the horn's two coaxial conductors made of aluminum alloy. The horn current pulse is approximately a half-sinusoid of amplitude 174 kA, 143 s long, synchronized to each beam spill. The polarity of the horn current flow can be (and has been) switched, in order to focus negatively charged mesons, and therefore produce an antineutrino instead of a neutrino beam. The beam of focused, secondary mesons emerging from the target/horn region is further collimated, via passive shielding, and allowed to decay into neutrinos in a cylindrical decay region filled with air at atmospheric pressure, 50 m long and 90 cm in radius. A beam absorber located at the end of the decay region stops the hadronic and muonic component of the beam, and only a pure neutrino beam pointing toward the detector remains, mostly from a pion to mu+ nuofmu decays.

## A.2 Resistive Wall Monitor

A resistive wall monitor measures the image charge that flows along the vacuum chamber following the beam. The image charge has equal magnitude but opposite sign. Depending on the beam velocity, the image charge will lag behind and be spread out along its path. The ultimate bandwidth of such a detector is limited by this spreading of the electric field lines between the beam and the inside walls of the beam pipe. The spreading angle is approximately 1/ gamma for relativistic beams ( gamma is the ratio of total energy to rest energy). The estimated bandwidth limit from spreading is 47 GHz at injection to the Main Injector for a 3 cm radius pipe and 8 GeV proton energy. In practice, the detector response is difficult to maintain above the microwave cutoff frequency of the beam pipe,measured to be 1.5 GHz for the elliptical beam pipe used in the Main Injector. Above cutoff, the characteristic impedance of the beam pipe and the impedance of nearby structures such as bellows or changes in geometry can effect accuracy.

In order to measure the image current, the beam pipe is cut and a resistive gap is inserted (Figure 1). Various ferrite cores are used to force the image current through the resistive gap rather than allowing it to flow through other conducting paths. In addition to image current, other currents are often found flowing along the beam pipe. The gap and cores are placed inside a metal can to shunt these “noise” currents around rather than through the resistive gap. The inductance of the cores and the resistance of the gap forms a high pass filter with a corner frequency of  $R/2\pi L$ , typically a few kilohertz. Above this frequency, cores act to minimize the net current through their center by inducing a current through the resistive gap that just cancels the beam current. The gap impedance is chosen to be well below the impedance of the cores inside the shielding can. Several types of ferrite and microwave absorbers are used to maximize the impedance and minimize resonances within the desired bandwidth. The Main Injector shielding can has an impedance greater

than 30 ohms with the ferrite cores. In parallel with the 1 ohm gap impedance, 30 ohms can cause frequency dependent errors of pm1.5% or 0.15 db. If the charge density around the circumference of the gap is not uniform, the voltage across the gap will vary around the circumference. The gap will act as an azimuthal transmission line transporting charge until the voltage equalizes. The time domain response of the detector would be distorted during this time. Position detectors have been made by exploiting this effect. The elliptical shape of the Main Injector pipe aggravates this problem (Figure 2). To overcome this problem, a round geometry is used for the gap and the signals from several monitor points equally spaced around the circumference are combined to form a single output.

# **Appendix B**

## **Employed CAMAC modules**

**B.1 USB Camac Controller**

**B.2 TDC**

**B.3 ADC**

